

# **Petrochronology of the Dom Feliciano Belt foreland in southernmost Brazil reveals two distinct tectonometamorphic events in the western central Kaoko–Dom Feliciano–Gariep orogen**

Matheus Ariel Battisti<sup>1</sup>, Jiří Konopásek<sup>2, 3</sup>, Maria de Fátima Bitencourt<sup>1</sup>, Jiří Sláma<sup>4</sup>, Jack James Percival<sup>2</sup>, Giuseppe Betino De Toni<sup>1</sup>, Stephanie Carvalho da Silva<sup>1</sup>, Elisa Oliveira da Costa<sup>1</sup>, Jakub Trubač<sup>5</sup>

1- Programa de Pós-graduação em Geociências, Instituto de Geociências, Universidade Federal do Rio Grande do Sul, Porto Alegre, Brazil

2- Department of Geosciences, UiT–The Arctic University of Norway, Tromsø, Norway

3- Czech Geological Survey, Prague, Czech Republic

4- Institute of Geology of the Czech Academy of Sciences, Prague, Czech Republic

5- Faculty of Science, Charles University in Prague, Czech Republic

Corresponding author: Matheus Ariel Battisti, [matheus.ariel.battisti@gmail.com](mailto:matheus.ariel.battisti@gmail.com)

Address: Av. Bento Gonçalves, 9500 – Porto Alegre, Rio Grande do Sul state, Brasil. IGEO – Universidade Federal do Rio Grande do Sul, Campus do Vale – Zip Code: 91501-970

## Abstract

The Dom Feliciano Belt is the South American part of an extensive Neoproterozoic orogenic system that developed during the late Cryogenian–early Cambrian close to the margin of southwest Gondwana. The link of its evolution with the tectonic processes in its African counterpart is still not well understood.  $P$ – $T$  estimates, Lu-Hf garnet–whole-rock ages, U-Pb monazite SIMS ages and REE garnet and monazite data from samples of the Porongos and Passo Feio complexes indicate diachronous tectonic evolution of the central Dom Feliciano Belt foreland. Metasedimentary rocks of the eastern Porongos Complex reached previously estimated metamorphic peak conditions of  $\sim 560$ – $580$  °C, 5.8–6.3 kbar at  $654 \pm 2$  Ma, based on Lu-Hf isochron garnet–whole-rock age data. This episode represents an early orogenic thickening in the foreland as a response to the beginning of the transpressive convergent evolution of the belt. The monazite age of  $614 \pm 6$  Ma (U–Pb SIMS) is interpreted as associated with post-exhumation magmatic activity in the foreland and suggests that the eastern Porongos Complex was exhumed sometime between ca. 660 and 615 Ma. The main metamorphic and deformation event in the Porongos Complex's western region occurred at  $\sim 545$ – $565$ °C and 4.3–5.3 kbar at  $563 \pm 1$  Ma (garnet– whole-rock Lu-Hf isochron age). The exhumation of this part of the foreland is dated by using monazite crystallising during garnet breakdown and suggests retrograde metamorphism at  $541 \pm 7$  Ma (U–Pb SIMS). The main metamorphic fabric in the Passo Feio Complex further to the west developed at  $571 \pm 2$  Ma (garnet– whole-rock Lu-Hf isochron age) at 560–580 °C and 4.7–6.4 kbar. The western part of the Porongos Complex and the Passo Feio Complex have deformed at similar  $P$ – $T$  conditions and apparent geothermal gradients at ca. 570–565 Ma. These regions record a second crustal thickening event in the Dom Feliciano Belt foreland and the orogenic front migration towards the west as a response to the onset of crustal thickening on the African side of this long-lived transpressive orogenic system.

**Keywords:** *Lu-Hf garnet-whole-rock dating, U-Pb monazite SIMS, crustal thickening, thermodynamic modelling, Dom Feliciano Belt*

## INTRODUCTION

Determination of the timing of metamorphic events is critical for correctly interpreting the evolution of orogenic belts. In metamorphic terranes with protracted evolution, separation of distinct deformation events from a progressive but single period of deformation is sometimes difficult due to the similar fabric superposition and comparable changes in the metamorphic mineralogy (e.g. Fossen et al. 2019). The petrochronological approach (Fraser et al. 1997) combines the application of various geochronometers with detailed petrological and microstructural observations to accurately link the appearance of various mineral phases used for geochronology with metamorphic–deformation events in a specific rock (Engi et al. 2017; Yakymchuk et al. 2017). Due to the different physical and chemical properties of each mineral, as is the diffusivity of the main elements or the specific closure temperature of their isotopic systems, various minerals such as zircon (e.g. Rubatto et al. 2006), monazite (e.g. Rocha et al. 2017), garnet (Baxter et al. 2017), titanite (Kohn 2017), allanite, xenotime or apatite (Engi 2017) can be utilized in petrochronological studies. Moreover, due to the specific physical properties of the datable minerals and the potential link of their crystallisation to various metamorphic and (micro)structural stages, it has become common to investigate more than one mineral (and isotopic system) in the same rock to interpret the pressure ( $P$ )–temperature ( $T$ )–deformation ( $d$ ) evolution of geological units of metamorphic terranes in time (Hermann and Rubatto 2003; Rubatto et al. 2006; Stevens et al. 2015; Hagen-Peter et al. 2016; Regis et al. 2016; Rocha et al. 2017; Schaltegger and Davies 2017; Walczak et al. 2017; Konopásek et al. 2019; Soret et al. 2019; Percival et al. 2022).

The Dom Feliciano Belt in SE South America (Fig. 1) is a long-lived Neoproterozoic belt built by protracted deformation. The complexity of its evolution is highlighted by recent papers, which have suggested that the contractional period lasted from ca. 660–640 Ma up to < ca. 570 Ma (e.g. Oriolo et al. 2016; Battisti et al. 2018; De Toni et al. 2020a, 2021; Percival et al. 2021, 2022, 2023; Hueck et al. 2022). The main purpose of this paper is to determine the timing of critical deformation events that shaped the present-day structure of the central Dom Feliciano Belt. Recent investigations in that area have suggested the thrusting of high-grade metamorphic rocks over the pre-orogenic supracrustal rocks of the foreland (Battisti et al. 2018; De Toni et al. 2021), as well as the burial of syn-orogenic sediments (e.g. Höfig et al. 2018). However, the timing and metamorphic conditions of these events are not yet well understood.

For this reason, two supracrustal metamorphic complexes of the central Dom Feliciano Belt foreland were studied and compared.  $P$ – $T$  estimates through thermodynamic modelling, Lu–Hf garnet–whole-rock isochron ages and U–Pb SIMS monazite ages from metasedimentary samples

provided metamorphic and geochronological data, which point to two separate and well-constrained periods of crustal thickening, both followed by periods of intense magmatic activity. The data provide evidence for the progressive migration of deformation towards the west, away from the centre of the orogenic system, and explain the recently discussed involvement of syn-orogenic sediments and magmatic rocks in the deformation of the central Dom Feliciano Belt foreland (Battisti et al. 2018, 2022; Höfig et al. 2018).

## **GEOLOGICAL SETTING**

### **Dom Feliciano–Kaoko–Gariep orogenic system**

The study area is located in the central Dom Feliciano Belt (Fig. 1 – DFB), which is the South American part of an NS-trending Neoproterozoic orogenic system also involving the Kaoko and Gariep belts along the Atlantic coast of southern Africa (e.g., Porada 1979; Gray et al. 2008; Konopásek et al. 2020). The Dom Feliciano Belt is the result of the Brasiliano/Pan-African cycle, which started at ca. 840–800 Ma by igneous activity and associated sedimentation interpreted by some authors as related to a continental arc (Koester et al. 2016; Martil et al. 2017; Battisti et al. 2018; De Toni et al. 2020a) or as generated in a back-arc/rift setting (Konopásek et al. 2018; Will et al. 2019; Hueck et al. 2022). The system evolved into a contractional tectonic regime, which started at ca. 660–640 Ma (e.g. Gross et al. 2006, 2009; Oyhantçabal et al. 2009; Lenz et al. 2011; Martil 2016; Peel et al. 2018; Will et al. 2019; De Toni et al. 2020a; Konopásek et al. 2020; Percival et al. 2021, 2022). The contraction continued until at least 580–550 Ma, as recorded by ongoing thickening and associated metamorphism of both forelands of the orogenic system (Frimmel and Frank 1998; Goscombe and Gray 2008; Höfig et al. 2018; Percival et al. 2022, 2023). Such a convergent period is related to the formation of the Gondwana supercontinent (e.g. Rapela et al. 2011; Ramos et al. 2017; Oriolo et al. 2017).

The central DFB outcrops in southernmost Brazil (Rio Grande do Sul state) and is usually divided into Western, Central and Eastern domains (Fragoso-Cesar et al. 1986; Fernandes et al. 1992; Basei et al. 2000) (Fig. 1c). The Western domain consists of Paleoproterozoic rocks (2.5–2.0 Ga - Hartmann et al. 2000) of the foreland basement, ophiolites reminiscent of an oceanic crust (920–890 Ma - Arena et al. 2016) and juvenile arc-related rocks of the São Gabriel Block (750–690 Ma - Lena et al. 2014) with associated metasedimentary complexes (e.g. the Passo Feio Complex - Bitencourt 1983).

The Central Domain is represented mainly by the Porongos Complex (PC), composed of low- to medium-grade volcano-sedimentary rocks (Jost and Bitencourt 1980; Saalman et al.

2005; Pertille et al. 2017) of Tonian (810–780 Ma) to Ediacaran (ca. 600 Ma) age (e.g. Saalman et al. 2011; Pertille et al. 2017; Höfig et al. 2018; Battisti et al. 2022) with locally exposed Paleoproterozoic basement (Encantadas Complex; 2.26–2.0 Ga – Hartmann et al. 2003; Philipp et al. 2008). Late-orogenic, Ediacaran to Ordovician volcano-sedimentary deposits extensively cover the foreland (Western and Central domain) (Oliveira et al. 2014; Paim et al. 2014).

The Eastern Domain represents the hinterland, and in the Rio Grande do Sul state, it features mainly granitic rocks (also called Pelotas Batholith - Fragoso-Cesar et al. 1986). The batholith is interpreted as part of a post-collisional granitic belt (Bitencourt and Nardi 1993; Bitencourt and Nardi 2000; Philipp and Machado 2002), whose emplacement was controlled by a large-scale discontinuity (Southern Brazilian Shear Belt - SBSB) active between ca. 650 and 580 Ma (Bitencourt and Nardi 2000; Nardi and Bitencourt 2007).

## **INSERT FIGURE 1**

### **Porongos Complex**

The Porongos Complex (PC) is part of the Dom Feliciano Belt foreland and comprises Neoproterozoic supracrustal rocks metamorphosed at lower greenschist to middle amphibolite facies conditions (Jost and Bitencourt 1980; Saalman et al. 2006; Pertille et al. 2017; Höfig et al. 2018; De Toni et al. 2021). The complex comprises metasedimentary and metavolcanic rocks, some ultramafic lenses and, less often, deformed granitic rocks (Jost and Bitencourt 1980; Marques et al. 2003; Zvirtes et al. 2017). Some authors interpret the ultramafic lenses as ophiolite remnants (Arena et al. 2018; Werle et al. 2020). The PC metamorphic grade increases from west to east. The Cerro do Facão staurolite-bearing metapelites at the easternmost border (Fig. 2) record the highest metamorphic grade of the complex (Jost and Bitencourt 1980; Lenz 2006). The peak PT conditions of these rocks were estimated at 560–580°C and 5.8–6.3 kbar (De Toni et al. 2021), and the only available metamorphic age is an imprecise age of  $658 \pm 26$  Ma (Lenz 2006; Rb–Sr in muscovite and whole-rock).

Provenance studies in the PC have shown two distinct sources of the metamorphosed clastic sediments (Gruber et al. 2011, 2016; Pertille et al. 2015b, 2015a, 2017; Höfig et al. 2018). Based on this data, Höfig et al. (2018) suggested that the precursor of the Porongos Complex could have been at least two distinct and diachronous basins. The older PC metasedimentary rocks are represented by the Cerro da Árvore sequence (*sensu* Jost and Bitencourt 1980). These are located mainly in the eastern part of the complex (Fig. 2 inset) and represent largely clastic infill of a pre-orogenic basin(s) (> 650 Ma). The younger PC basin, called the Capané sequence, is

related to the syn-orogenic (< ca. 650 Ma) evolution, as discussed by Höfig et al. (2018) and Battisti et al. (2018, 2022). In the western part of the PC (Fig. 2), the syn-orogenic sedimentary rocks are interleaved with the rocks of the pre-orogenic PC basin(s) (Höfig et al. 2018). Associated intermediate to acid metavolcanic rocks also yielded contrasting ages in different parts of the complex. Eastern regions of the PC contain metavolcanic rocks with protolith ages of ca. 770–800 Ma (Saalman et al. 2011; Pertille et al. 2017; Battisti et al. 2022), whereas studies of meta-volcano sedimentary rocks in the western portion of the complex (Höfig et al. 2018) reported magmatic ages of ca. 600 and 601 Ma (LA–MC–ICP–MS, U–Pb zircon). Such a dataset shows that the igneous activity and late sedimentation in the northwestern PC are younger than the metamorphic peak recorded in the eastern portion of the PC ( $658 \pm 26$  Ma - Lenz 2006). According to the data compiled by Battisti et al. (2022), these two diachronous basins (Cerro da Árvore and Capané sequences) are separated by the main W-verging thrust fault in the Porongos Complex called Santana da Boa Vista thrust fault (Jost and Bitencourt 1980). The metamorphosed pre-orogenic sediments appear mostly east of the fault, whereas the relics of the syn-orogenic basin appear exclusively west of the fault, in the northwestern part of the Porongos Complex.

Recent papers suggested that a part of the pre-orogenic basin of the PC (Cerro da Árvore sequence) and a part of the Várzea do Capivarita Complex may have shared a similar sedimentary depositional environment in their pre-collisional setting (Martil et al. 2017; Battisti et al. 2018, 2022). Battisti et al. (2022) argued that both complexes share igneous rocks with the same ca. 780 Ma protolith age, identical REE geochemistry, similar isotopic Nd–Sr and oxygen signatures, similar structural evolution, and convergent *P–T–t* evolution. These similarities led Battisti et al. (2018, 2022) and De Toni et al. (2021) to conclude that the higher grade, deeper VCC hinterland rocks were thrust over the lower grade, shallower PC foreland during a ca. 650 Ma collisional event.

## **INSERT FIGURE 2**

### **São Gabriel Block**

#### **São Gabriel Block overview**

The São Gabriel Block (Fig. 1 and 2) represents the largest occurrence of juvenile magmatic rocks in the DFB (e.g. Arena et al. 2017, 2016; Lena et al. 2014; Saalman et al. 2007, 2005). Although many authors do not consider the São Gabriel Block as part of the Dom Feliciano Belt and interpret it as a tectonic unit resulting from an independent orogeny (e.g. Chemale 2000; Philipp et al. 2016b; Arena et al. 2017), there seems to be a consensus that its long-lived history

also influenced the evolution of the DFB (Philipp et al. 2016; Konopásek et al. 2018; De Toni et al. 2020a).

According to Arena et al. (2016), some igneous rocks of the block may represent part of an oceanic domain (ophiolites - 920–890 Ma), accreted to a juvenile arc (ca. 880 Ma Passinho event of Leite et al., 1998) that evolved towards a continental magmatic arc (770–690 Ma - Lena et al. 2014). The oceanic closure is interpreted to have happened between 690–650 Ma (Lena et al. 2014) or 650–600 (Arena et al. 2017), whereas late granitic magmatism took place at ca. 585 Ma (Arena et al. 2017). The São Gabriel Block structural framework features NE-striking planar fabrics, predominantly dipping NW at low to medium angles, reworked by oblique, SE-verging, plus dextral transpression (Saalman et al. 2005).

Metagneous, arc-related rocks of the São Gabriel Block are surrounded by metamorphic supracrustal complexes, both covered by extensive Ediacaran sedimentary basins. The intrinsic characteristics of such complexes (Pontas do Salso, Cambaí, Bossoroca, Imbicuí and Passo Feio - Philipp et al. 2021 and references therein) are beyond the scope of this work. The exception is the Passo Feio Complex, introduced in detail below.

### **Passo Feio Complex**

The Passo Feio Complex (PFC) is traditionally considered the easternmost unit of the São Gabriel Block (Fig. 1, 2), separated from the easterly Porongos Complex by a magnetic anomaly (Costa 1997) whose meaning is, however, unclear because its area is covered by post-orogenic sediments (Fig. 2). This has led some authors to interpret the anomaly as a manifestation of a suture (Fernandes et al. 1995; Costa 1997), whereas others (Costa et al. 2021) interpret it as a regional dextral shear zone. As no other data would confirm this magnetic anomaly as a suture, the relation between the Passo Feio Complex and the rocks to the east (Central and Eastern domains) remains uncertain, as does the eastern limit of the São Gabriel Block.

The PFC comprises phyllites, metapelitic schists, amphibole-bearing rocks such as amphibolites, metagabbros and amphibole schists, acid to intermediate metavolcanoclastic rocks, and subordinate magnesian schists and marble lenses (Bitencourt 1983; Bitencourt and Hartmann 1984a, 1984b; Costa et al. 2021; Hoerlle et al. 2022). The acid metavolcanic rocks from the northern region display protolith ages of ca. 580 Ma (Battisti et al. 2023), whereas the age of the metabasic rocks remains unknown. The PFC crops out as an antiformal structure with a subhorizontal axis plunging either NNE or SSW (Costa et al. 2021) with the  $562 \pm 8$  Ma (SHRIMP U–Pb zircon - Remus et al. 2000) calc-alkaline Caçapava Granite in its core. The PFC is



surrounded by the Ediacaran to Cambrian volcano-sedimentary sequences of the Camaquã Basin (Oliveira et al. 2014; Paim et al. 2014 - Fig. 2) and at the northeast by the Paraná Basin.

The main metamorphic fabric of the complex has developed during progressive deformation (Bitencourt 1983; Costa et al. 2021) coeval with the growth of garnet up to the peak metamorphic conditions. The peak conditions were estimated by Costa et al. (2021) at 560–570 °C and 5–5.5 kbar for a garnet–staurolite schist and at 500–510 °C and 5–6.4 kbar for a garnet phyllite. The main fabric is overprinted by a second metamorphic event marked by the crystallisation of andalusite (Costa et al. 2021), which was temporally close to the emplacement of the Caçapava Granite (Bitencourt 1983). The localized foliation related to such second metamorphic phase shows mainly recrystallization of biotite and relic minerals of the metamorphic peak schist, which indicates that the latter reached intermediate greenschist facies (biotite zone) with pressures lower than ~ 4 kbar, as indicated by the crystallisation of andalusite (Costa et al. 2021).

Geochronological data for the PFC's first metamorphic event are rather limited and obscure. A single SHRIMP spot in a zircon rim of  $685 \pm 12$  Ma (Remus et al. 2000) was associated with the metamorphic peak (probably a mixed age – see discussion). On the other hand, the age of the second metamorphic event is better constrained as this metamorphism was interpreted to be contemporary to the emplacement of the Caçapava Granite at ca. 562 Ma (see above - Remus et al. 2000).

Provenance studies in PFC are also scarce. The available data of four PFC metasedimentary rocks (Lopes et al. 2015) indicated ages of 3.4–3.3 Ga, 2.4–2.3 Ga, 2.0 Ga, 1.8–1.7 Ga and 850–800 Ma for the main source areas (zircon U-Pb SHRIMP).

## RESULTS

### Sample description and estimates of metamorphic conditions

Metamorphic conditions for the Porongos Complex eastern region were published by De Toni et al. (2021), and we will use their results for further discussion of the evolution of the Dom Feliciano Belt foreland. To quantify the metamorphic evolution of the northwestern region of the Porongos Complex and the evolution of the Passo Feio Complex, the conditions of equilibration of mineral assemblages in two mica schist samples (MAB56A and BD03) were modelled by calculating  $P$ – $T$  pseudosections based on the whole-rock chemical composition and H<sub>2</sub>O component in excess. Due to the absence of minerals with elevated content of Fe<sup>3+</sup>, all Fe in the samples was considered as FeO. The stability of the mineral assemblages was modelled using *Perple\_X* 6.8.9 software (Connolly 2005, 2009) and thermodynamic properties of mineral



endmembers published by Holland and Powell (2011). The mixing properties of the minerals were taken from Fuhrman and Lindsley (1988) for feldspar and White et al. (2014) for biotite, white mica, chlorite, staurolite, chloritoid, cordierite and garnet.

Whole-rock compositions were obtained from rock powder tablets using a Rigaku RIX 2000 X-Ray Fluorescence analyser at the X-ray Fluorescence Laboratory of Universidade Federal do Rio Grande do Sul (UFRGS), Brazil and at AcmeLabs - Bureau Veritas Minerals in Canada. Mineral compositions were determined at the Microprobe Laboratory, CPGq, UFRGS, Brazil and the Laboratory of Electron Microscopy and Microanalysis of the Masaryk University in Brno, Czech Republic, using the Cameca SXFive microprobe at analytical conditions of 15 keV, 15 nA current, and beam size of 5  $\mu\text{m}$ . The instrument was calibrated using diopside (Ca, Mg), rhodonite (Mn), sanidine (Si, K, Al), Fe<sub>2</sub>O<sub>3</sub> (Fe), albite (Na), rutile (Ti) and Cr<sub>2</sub>O<sub>3</sub> (Cr) as standards. The crystals used during the microprobe analyses were PET for Ca, Cr, Ti e K; TAP for Si, Mg, Al e Na; and LIF for Fe and Mn. A compositional profile was measured for one garnet crystal in each sample (see supplementary data) together with individual core and rim analyses that were later used for *P–T* condition estimates (Table 1 and supplementary data). Mineral abbreviations used throughout this paper are after Whitney and Evans (2010).

### **MAB56A – Northwestern region of the Porongos Complex**

Sample MAB56A (30.4767° S; 52.9818° W – all coordinates in WGS84 – Fig. 2) is a garnet-bearing mica schist with the main mineral assemblage garnet–biotite–plagioclase–muscovite–quartz–ilmenite (Fig. 3a, b) from the structural footwall of the Santana da Boa Vista thrust fault in the northwestern part of the Porongos Complex, where the pre-orogenic metasedimentary rocks were tectonically interleaved with the syn-orogenic flysch sediments (Höfig et al. 2018; Battisti et al. 2022). The schistosity is marked by alternating muscovite-rich and quartz-plagioclase-rich layers, both intensely microfolded. The lepidoblastic texture and shape preferred orientation of muscovite (~40 vol.%) with crystal sizes up to 2 mm mark the main schistosity. Muscovite contains 3.01–3.08 a.p.f.u. of Si and 0.02–0.14 a.p.f.u. of Ti. Quartz and plagioclase are fine-grained (up to 0.4 mm) and display lenses with intergranular interlobate texture. Quartz and plagioclase comprise ~45% of the rock volume. Plagioclase is albite (An<sub>0–2</sub>) with <1 mol.% of K-feldspar component. Biotite (~10 vol.%) crystals are up to 0.5 mm long with lepidoblastic texture in mica-rich layers. Biotite shows  $X_{\text{Mg}}$  between 0.31 and 0.35, 0.09–0.16 a.p.f.u. of Ti and 1.33–1.45 of Al<sup>IV</sup>.

Garnet (~3 vol.%) shows variable shapes in the thin section. Some crystals appear as fragments in the rock matrix (Fig. 3a), whereas others form mostly equant, up to 5 mm large

porphyroblasts, usually cracked and partly consumed along the edges. They rarely show sigmoidal quartz and ilmenite inclusion trails that mark the porphyroblast rotation relative to the external matrix foliation during growth (Fig. 3b). In the fractures, chlorite commonly grows due to garnet dissolution (Fig. 9g and h). Garnet grains show strong chemical zoning, with increasing pyrope and almandine components from core to rim compensated by decreased grossular and spessartine components. General garnet core-to-rim composition (mol.%) is Alm<sub>67–82</sub>, Py<sub>5–10</sub>, Grs<sub>14–5</sub>, Sps<sub>16–2</sub>. The  $X_{Mg}$  value calculated as Mg/(Mg+Fe) (based on a.p.f.u.) increases from 0.07 to 0.11 from core to rim (Table 1, 2).

Chlorite (~2 vol.%) crystals are up to 0.3 mm long, and they occur as both dispersed in the rock matrix and in cracks and pressure shadow tails of garnet porphyroblasts. Chlorite  $X_{Mg}$  varies from 0.36 to 0.39. Most of the chlorite is interpreted to have formed after the metamorphic peak by a retrogressive reaction that consumed garnet and some biotite in the matrix; however, it cannot be excluded that some chlorite crystals intergrown with mica in the matrix represent a part of the mineral assemblage stable at the metamorphic peak. Accessory minerals are tourmaline, apatite, monazite, and zircon.

The overall microstructure with intense microfolding in the matrix, garnet fragmentation and fracturing accompanied by the growth of late chlorite points to some degree of post-peak metamorphic reworking of the sample.

### **INSERT FIGURE 3**

The P–T pseudosection calculated for sample MAB56A (Fig. 4, bulk composition in mass proportions: SiO<sub>2</sub> – 62.15; Al<sub>2</sub>O<sub>3</sub> – 18.34; TiO<sub>2</sub> – 1.11; FeO – 8.14; MnO – 0.14; MgO – 1.96; CaO – 0.89; Na<sub>2</sub>O – 0.45; K<sub>2</sub>O – 3.23; H<sub>2</sub>O saturated) indicates that the assemblage Chl + Grt + Ms + Bt + Qz + Pl + Ilm is stable approximately at 490–560°C, and in the pressure range of 1.5 to 5.3 kbar. Conditions of early garnet growth were established at 520–540°C and 3.9–5.3 kbar (Fig. 4a) by using the garnet core composition without applying the fractionation routine (Table 2). However, some garnet grains represent relics of larger porphyroblasts consumed by retrograde reactions. Such observation suggests that the rims of the least re-equilibrated porphyroblasts that survived the retrogression may represent higher metamorphic conditions than the matrix assemblage. The estimate of peak metamorphic conditions attained by the sample has been made using the garnet fractionation routine available in the Perple\_X software (Connolly, 2005) to eliminate the composition of the garnet cores from the bulk chemistry of the sample. The calculation results show that isopleths for garnet rim endmembers and  $X_{Mg}$  of biotite overlap at 545–565°C and 4.3–5.3 kbar in the staurolite stability field (field 21 – figure 4b). Thus, such data

suggest that staurolite might have been present at the metamorphic peak and then all consumed during retrogression. The same is observed in figure 4a, where even without eliminating garnet core composition from the bulk rock chemistry, the garnet rim composition partly crosses the staurolite-in curve. A comparison of the observed vs. modelled mineral compositional parameters from all studied samples is shown in Table 2.

**INSERT FIGURE 4**

**INSERT TABLE 1**

**INSERT TABLE 2**

### **BD03 - Passo Feio Complex**

Sample BD03 (30.64389° S; 53.45345° W) is a muscovite–garnet–staurolite–biotite–plagioclase–quartz schist (Fig. 3c, d) collected in the southern part of the Passo Feio Complex (Fig. 2). The schistosity is marked by alternating mica-rich and quartz-rich bands (Fig. 3c). Mica-rich bands are discontinuous, up to 1 mm thick and composed of lepidoblastic biotite (~25 vol.%) and muscovite (~5 vol.%) up to 1.5 mm in length, and locally chlorite (~1 vol.%). Muscovite contains 3.01–3.04 a.p.f.u. of Si and 0.02 a.p.f.u. of Ti, whereas biotite shows  $X_{Mg}$  between 0.44–0.51, 0.04–0.10 a.p.f.u. of Ti and 1.26–1.32 of  $Al^{IV}$ . Chlorite has  $X_{Mg}$  of 0.51–0.53. Quartz-rich bands also contain some fine-grained (0.05 to 1 mm) plagioclase with inequigranular seriate texture (both adding up to ~45 vol.%). Plagioclase is andesine ( $An_{31-33}$ ) with <1 mol.% of K-feldspar component. The opaque phase is ilmenite and represents ~2 vol.%.

The external foliation wraps around the garnet and staurolite porphyroblasts, and their pre-syn-tectonic origin is suggested by the rotation of their internal foliation highlighted by opaque minerals and quartz inclusions. Staurolite porphyroblasts (~15 vol.%;  $X_{Mg} = 0.16-0.20$ ) are up to 3.5 mm large and appear mostly in the mica-rich layers. Garnet (~8 vol.%) forms 0.8–1.5 mm large equant grains, usually with internal cracks (Fig. 3d). Such grains usually contain quartz and ilmenite inclusions and pressure shadows made up of biotite, muscovite, and quartz. Garnet grains show a strong chemical zoning with increasing almandine component from core to rim compensated by decreased spessartine component. On the other hand, grossular and pyrope display very weak chemical zoning. General garnet core-to-rim composition (mol.%) is  $Alm_{64-75}$ ,

Prp<sub>7-11</sub>, Grs<sub>11-6</sub>, Sps<sub>20-7</sub>. The  $X_{Mg} = 0.10-0.13$  is almost constant from core to rim. Other accessory phases are represented mainly by tourmaline and zircon.

*P-T* pseudosection calculated for sample BD03 (bulk composition in mass proportions: SiO<sub>2</sub> – 64.13; Al<sub>2</sub>O<sub>3</sub> – 15.61; TiO<sub>2</sub> – 0.96; FeO – 7.95; MnO – 0.12; MgO – 3.13; CaO – 1.53; Na<sub>2</sub>O – 1.81; K<sub>2</sub>O – 2.60; H<sub>2</sub>O saturated) is presented in figure 5. The estimate of peak metamorphic conditions has been made using the garnet fractionation routine available in the *Perple\_X* software (Connolly, 2005). The reason for the subtraction of the garnet interior from the bulk is that the garnet shows strong chemical zonation from core to rim, which, together with its high modal proportion (~8 vol.%), may influence the effective composition available during peak metamorphic conditions (Stuwe 1997; Lanari and Engi 2017). Garnet core conditions were established at 525–545°C and 4.1 – 4.5 kbar (Fig. 5a) without applying the fractionation routine (Table 2). Several fractionation paths with different slopes in the *PT* space were tested (always crossing the garnet core conditions) to find the *PT* conditions at which the modelled final garnet composition successfully reproduced the observed composition of the garnet rim in the sample. Four fractionation paths met such conditions, and all of them led to similar results (Fig. 5a, b), which indicate that the assemblage Chl + Grt + Ms + St + Bt + Pl + Qz + Ilm was stable at ~560–600°C and above 4.7 kbar (Fig. 5b). Isopleths for garnet rim endmembers, in addition to  $X_{Mg}$  in staurolite and biotite, and  $X_{An}$  in plagioclase, suggest equilibration conditions at 560–580°C and 4.7–6.5 kbar.

## **INSERT FIGURE 5**

### **MAB51B – Eastern region of the Porongos Complex**

A third mica-schist sample was studied to estimate the timing of metamorphic evolution in the eastern Porongos Complex. The metamorphic conditions of this region were estimated for sample MAB52A by De Toni et al. (2021). As this sample had no monazite, the geochronological study was conducted using sample MAB51B from a nearby locality.

Sample MAB51B (30.73782° S, 52.81326° W) is a garnet-plagioclase-biotite-muscovite schist (Fig. 3e) collected in the hanging wall of the Santana da Boa Vista thrust fault, eastern part of the Porongos complex (Fig. 2). The schistosity is marked by lepidoblastic muscovite (~65 vol.%) and biotite (~15 vol.%). Both types of mica form crystals up to 0.5 mm long and commonly display isoclinal microfolds and undulose extinction. Plagioclase (~8 vol.%), quartz (~2 vol.%), and accessory K-feldspar (<<1 vol.%) form lenses of fine-grained (0.06–0.2 mm) inequigranular texture. Garnet (~5 vol.%) forms 3-4 mm large isometric grains, usually with well-developed

crystal faces and internal cracks. Chlorite (~3 vol.%) forms isolated, ~1 mm long individual clusters interpreted as late overgrowths on muscovite-biotite crystals. Rare tiny staurolite crystals (<0.05 mm, <1 vol.%) were found by SEM. The opaque phase is ilmenite (~1 vol.%).

The mineral paragenesis (staurolite-garnet-biotite-muscovite ± plagioclase) and the texture of MAB51B resemble those described for sample MAB52A of De Toni et al. (2021). These samples represent the same lithological unit and thus likely display similar metamorphic peak conditions of ~560–580 °C and 5.8–6.3 kbar (De Toni et al. 2021). Another important similarity between both samples is that the staurolite crystals are strongly replaced by muscovite (Fig. 3f). The main differences are: i) staurolite is more abundant in MAB52A than in MAB51B; ii) Modal content of muscovite is higher in MAB51B than in the MAB52A sample (~65% vs 50%); iii) De Toni et al. (2021) did not report plagioclase in MAB52A.

### **Lu-Hf garnet geochronology and trace elements chemistry**

Lu-Hf garnet-whole-rock isochron ages were obtained for the three studied samples to provide a temporal framework for the metamorphic evolution of the central Dom Feliciano Belt foreland (Table 3, figure 6). In addition, REE and additional trace elements (Hf, U, Ti, Nd – see supplementary file) were analysed along transects across garnet to determine the potential influence of inclusions on bulk mineral, separate isotopic systematics and the influence of zonation on age interpretation. The results of trace element analysis are summarized in figures 7, 8 and 9, and complete data are available in supplementary files. Complete analytical methods for the Lu-Hf isotopic dating are described in appendix 1. Standards reproducibility and constants used for the Lu-Hf isochron calculations are given in the footnote to Table 3.

**INSERT TABLE 3**

**INSERT FIGURE 6**

#### **MAB51B – Eastern region of the Porongos Complex**

Lu-Hf isotopic analysis of sample MAB51B yielded a garnet-whole-rock isochron age of 654 ± 2 Ma, based on four garnet aliquots and one representative whole-rock powder aliquot (Fig. 6a).

Rim-to-rim profiles of two garnet crystals in this sample were analysed for REE and trace element contents. The REE data present an almost homogeneous pattern for all analysed spots (Fig. 7a). The data demonstrate a well-known (e.g. Hacker et al. 2019; Rubatto et al. 2006) enrichment of Heavy Rare Earth Elements (HREE – 10<sup>2</sup> to 10<sup>3</sup> ppm) over Light Rare Earth

Elements (LREE –  $10^{-3}$  to  $10^1$  ppm). Although garnet cores are somewhat enriched in LREE compared to garnet rims, and HREE concentrations increase slightly towards the rims, this variation is not systematic. The data in figure 7 also indicate a slightly negative europium anomaly  $\text{Eu}/\text{Eu}^* [(\text{Eu}_{\text{norm}})/(\text{Sm}_{\text{norm}} \times \text{Gd}_{\text{norm}})^{0.5}]$  ranging from 0.26 to 0.60, for garnet 1 and 0.24 to 0.60, for garnet 2 (see details in supplementary file).

The Lu profile is rather flat, with a slightly higher concentration in the garnet core and an anomalous enrichment in the right-hand outermost rim (Fig 8a). Hf shows peaks that coincide with peaks in U, suggesting the presence of zircon inclusions. The presence of ilmenite inclusions is also indicated by peaks of Ti (Fig. 8a). Considering the clean part of the garnet crystal (without mixed analyses from mineral inclusions), Lu shows a mean value of ~33 ppm and Hf ~0.1 ppm. All isotopic and trace element data are available as supplementary material.

## **INSERT FIGURE 7**

### **MAB56A – Northwestern region of the Porongos Complex**

Lu–Hf isotopic analysis of six garnet aliquots and two representative whole-rock powder aliquots yielded a garnet–whole-rock isochron age of  $563 \pm 1$  Ma for sample MAB56A (Fig. 6b).

In the thin section, two crystals (garnet 3 and 4) were selected for REE data acquisition by LA–ICP–MS. The REE patterns show mild enrichment in LREE of the rim over the core, whereas the core is strongly enriched in HREE.  $\text{Eu}/\text{Eu}^*$  values for garnet 3 range from 0.69 to 1.56 and from 0.59 to 0.78 for garnet 4 (Fig 9a).

Garnet 3 presents complex zoning of Lu with several peaks in different crystal growth zones (Fig. 8b). Several Hf+U peaks suggest the presence of zircon inclusions, whereas inclusions of ilmenite are evident from numerous peaks in Ti. In the clean garnet 4, Lu shows a mean value of ~32 ppm and Hf ~0.1 ppm.

## **INSERT FIGURE 8**

## **INSERT FIGURE 9**

### **BD03 – Passo Feio Complex**

For sample BD03, Lu–Hf isotopic analysis of four garnet aliquots and one representative whole-rock powder aliquot yielded a garnet–whole-rock isochron age of  $571 \pm 2$  Ma (Fig. 6c).



The analysed garnet in sample BD03 displays a general enrichment in Lu towards the right-hand side of the profile through the crystal (Fig. 8c). The appearance of Hf + U, Ti and U + Nd peaks suggests the presence of zircon, ilmenite and monazite/allanite inclusions, respectively. Lu shows a mean value of ~7 ppm and Hf ~0.1 ppm in the regions not affected by inclusions.

### **U–Pb SIMS monazite geochronology and trace elements chemistry**

Monazite crystals were separated from samples MAB51B and MAB56A, whilst no monazite was found in sample BD03. The monazite age was determined by U–Pb isotopic dating using Secondary Ion Mass Spectrometry (SIMS) at the NordSIMS facility hosted by the Swedish Natural History Museum in Stockholm. REE data for monazite were acquired by LA–ICP–MS in individual monazite grains (in mount – near spots previously analysed for U–Pb age dating) to compare their chemistry with that of garnet. These data were completed by concentration maps for selected trace elements to understand their spatial distribution in the analysed grains. Details of both separation and analytical methods are provided in appendix 1.

#### **MAB51B – Eastern region of the Porongos Complex**

Monazite extracted from sample MAB51B forms irregular grains up to 200  $\mu\text{m}$  large, which display various zoning patterns in back-scattered electron (BSE) images (Fig. 7). Most grains show well-preserved sector or oscillatory zoning related to crystal growth; however, zoning in some grains is more irregular. SEM imaging of monazite crystals in the thin section revealed either single crystals in the matrix (Fig. 7e, f) or grains apparently crystallized during the replacement of some other mineral (Fig. 7g).

Seventeen SIMS isotopic analyses were performed in thirteen different monazite grains, and the resulting data are plotted in a conventional Wetherill U–Pb concordia diagram. Considering all data, the 17 spots yielded a pooled concordia age of  $614 \pm 6$  Ma ( $2\sigma$ ), which we consider the monazite crystallisation age in the sample (Fig. 7d).

REE data normalised to chondrite (Boyton 1984) show enrichment of LREE over HREE (Fig. 7b). A pronounced Eu/Eu\* anomaly ranges from 0.007 to 0.040. Th/U ratios of the grains range between 13.3 and 46.2, with one outlier of 70.8.

#### **MAB56A – Northwestern region of the Porongos Complex**



Monazite separated from sample MAB56A is up to 200  $\mu\text{m}$  large (Fig 9). The crystals are usually rounded and cracked, displaying mostly weak zoning in BSE images. Concentric zoning is observed in some crystals, and two crystals preserve a central part rich in inclusions with a darker colour. However, from the observed zoning patterns, we cannot determine whether the crystals represent new monazite growth or are pre-existing crystals isotopically re-equilibrated during some post-growth metamorphic process. In the thin section, monazite is found in garnet cracks together with chlorite (Fig 9e-h), which suggests that the timing of monazite growth is closely related to the destabilization of garnet during retrogression. However, the monazite crystals in the garnet cracks are approximately ten times smaller than those analysed by SIMS (Fig. 9c). Monazite from that specific microstructural position was not dated due to its small grain size, and it is thus possible that it represents a different monazite-forming event. However, the dated large crystals all show very homogeneous U–Pb isotopic composition, resulting in a homogeneous cluster of data (Fig. 9d), which does not suggest more than one monazite-forming/modifying event.

Sixteen SIMS isotopic analyses were performed in eleven monazite grains of the sample. The data were plotted in the Wetherill U–Pb concordia diagram (Fig 9d), yielding a pooled concordia age of  $541 \pm 7$  Ma ( $2\sigma$ ).

REE data of monazite normalized to chondrite (Boyton 1984) show enrichment of LREE over HREE (Fig. 9a). Although the LREE concentration is rather homogeneous in all analysed grains, they show a strong variation in HREE content. A small Eu/Eu\* anomaly ranges from 0.36 to 0.63). Th/U ratios range between 2.2 and 26.0.

## **DISCUSSION**

### **Garnet and monazite petrochronology**

#### **MAB51B – Metamorphic peak in the eastern Porongos Complex (ca. 660 Ma)**

In sample MAB51B, garnet displays a homogenous REE pattern for both rim and core, suggesting equilibrium with stable minerals in the matrix during its growth (Lanari and Engi 2017). Furthermore, the weak Eu anomaly recorded by the garnet (Eu/Eu\* 0.24 to 0.60) likely suggests its growth in equilibrium with the matrix plagioclase. The Lu-Hf isochron age suggests that the metamorphic event responsible for garnet growth occurred at  $654 \pm 2$  Ma.

Trace element data suggest mild enrichment of Lu in garnet core (Fig. 7a). In metamorphic rocks, Lu usually shows partitioning into garnet core relative to rims due to Rayleigh fractionation.

Consequently, the Lu-Hf bulk garnet age is biased towards early garnet growth (e.g. Baxter and Scherer, 2013). In our case, the weak Lu enrichment in the centre of the profile either means that this element is more homogeneously distributed than in typical prograde garnet or that the analysed section did not reach the very core of the crystal. Thus, the above-reported garnet age should be considered an average age for garnet growth in sample MAB51B. The mean Hf content acquired by LA-ICP-MS analysis of clean garnet (<1 ppm) presents a discrepancy compared to the value found from garnet isotope dilution (4 ppm – Table 3). Such disparity is likely attributed to contamination from Hf-rich accessory mineral inclusions in garnet. The presence of zircon and ilmenite micro-inclusions in garnet is confirmed by spikes in U + Hf and Ti, respectively, in figure 8. Despite efforts to reduce the presence of such inclusions in garnet (after Anczkiewicz et al. 2004), some Hf-rich inclusions may have dissolved together with the garnet. However, as in the case of zircon inclusions, a huge Hf contamination would swipe off the isochron, which seems not the case, as all analyses stay aligned. Thus, it is most likely that the Hf contamination was generated by some other ‘low-Hf’ mineral than zircon, for example, ilmenite, which would not pose any problems to the age estimates. This age estimate overlaps within error with an unpublished Rb–Sr white mica/whole-rock age of  $658 \pm 26$  Ma from the same region (Lenz 2006).

The peak conditions of the metamorphic event responsible for garnet growth in the eastern Porongos region were estimated by De Toni et al. (2021) at  $\sim 560\text{--}580$  °C and 5.8–6.3 kbar, with the early growth of garnet at  $\sim 555\text{--}565$  °C and 5.4–5.7 kbar. Also, Lenz (2006) constrained the metamorphic peak of the region at  $\sim 590$  °C at 5–6 kbar (Table 4). The rocks studied by these authors display mineralogy identical to the sample MAB51B. We thus adopt the *P–T* data for the sample MAB52A of De Toni et al. (2021) as representing the peak of metamorphism in the region. The age of  $654 \pm 2$  Ma obtained for the garnet growth in MAB51B is thus interpreted as dating the prograde metamorphic event in the region.

### **MAB51B – Post-exhumation evolution of the eastern Porongos Complex (ca. 615 Ma)**

Monazite in sample MAB51B displays a generally homogenous REE pattern, with only some spread in the HREE content for individual grains. Such variation in HREE can be interpreted as local heterogeneities in rock chemistry or a time-related HREE zoning. The first possibility seems to be more likely, as the individual U–Pb dates form a homogeneous cluster in the concordia diagram (Fig. 7d). Thus, we interpret that all the analysed monazite grains represent the same event of monazite growth and the observed HREE variation may reflect a variable availability of HREE in the rock.

Monazite grains in this sample present an extremely pronounced Eu anomaly ( $\text{Eu}/\text{Eu}^* = 0.040$  to  $0.007$ ). Usually, such highly negative Eu anomaly is interpreted to represent monazite growth in equilibrium with plagioclase during melt crystallisation (Rubatto et al. 2006; Johnson et al. 2015; Hagen-Peter et al. 2016). This is also common in high-grade, migmatitic metamorphic rocks (e.g. Rubatto et al. 2013; Johnson et al. 2015; Hagen-Peter et al. 2016), but not the case for our lower-amphibolite facies schist. Moreover, the Eu anomaly in monazite is much stronger than that found in the garnet of the same sample (Fig. 7a, b), suggesting that the monazite did not grow during the garnet-forming metamorphic event (e.g. Rubatto et al. 2006).

Calculated distribution coefficients of REE between monazite and garnet (Fig. 10a, b) may be used as another proxy for interpreting the mutual stability of these two minerals during their growth.  $K_d$  curves were calculated for the REE content of each analytical spot in monazite divided by the REE content of one representative spot for each garnet region (core, mantle and rim; for values, see supplementary data file). The  $K_d$  values for garnet 1 (Fig 10a) and garnet 2 (Fig 10b) of sample MAB51B show similar results for all three garnet regions. Although the LREE distribution coefficients are in the range expected for equilibrium growth by previous studies (Hermann and Rubatto 2003; Rubatto et al. 2006; Warren et al. 2019), the MREE and HREE present lower (to much lower – e.g. Eu) distribution coefficients than expected for monazite which would crystallise in equilibrium with garnet. Such results may be seen as another indication that the garnet and monazite of sample MAB51B did not crystallise in equilibrium.

All the data presented and discussed above point to a monazite-forming event postdating the metamorphic peak reached by the schists of the eastern Porongos Complex. A significant activity of fluids altering the peak metamorphic assemblage is widespread in the region of sample MAB51B, as documented by muscovite halos replacing staurolite crystals and growth of andalusite crystals up to 10 cm in size in staurolite schists of the region (Lenz 2006; De Toni et al. 2021), or by the high density of quartz veins close to the nearby Passo do Marinheiro Fault. Thus, we interpret the large Eu anomaly found in the dated monazite from this sample as reflecting the growth of crystals triggered by Eu-depleted fluids.

The fluids were likely released during crystallisation of the nearby magmatic rocks. The Encruzilhada Granite is the closest; however, it assimilates ca. 580 Ma syenitic rocks (Padilha et al. 2019), and thus, it is too young to be the fluid source. On the other hand, the  $609 \pm 2$  Ma pulse of the multiphase Piquiri Syenite Massif (Rivera 2016; Sbaraini et al. 2020), which has also caused local contact metamorphism in the PC rocks (Battisti et al., 2018), is the most likely fluid source. Furthermore, K-feldspar may show a stronger Eu positive anomaly than plagioclase (Bea et al. 1994), and feldspar-rich magmatic rocks tend to concentrate Eu in the primary feldspar (Larsen 2002; Gahlan et al. 2016), which in turn may lead to the release of strongly Eu-depleted fluid

during their crystallization. Therefore, we interpret the  $614 \pm 6$  Ma monazite crystals as dating the time of the release of fluids from crystallizing syenitic rocks in the close vicinity, as their respective ages overlap within error. Furthermore, we associate the monazite growth with other features, such as the post-kinematic andalusite growth or the staurolite replacement by muscovite coronas (De Toni et al. 2021). Together with the Lu-Hf garnet age, these features suggest that the eastern Porongos Complex was exhumed between ca. 660–615 Ma since the syenite intruded it at shallower levels than those established for the metamorphic peak in the Porongos eastern region.

## **INSERT FIGURE 10**

### **MAB56A – Metamorphic peak in the northwestern Porongos Complex (ca. 560 Ma)**

In sample MAB56A, relict garnet grains present a systematic variation of HREE content, where the HREE are strongly enriched in garnet cores, and the concentrations decrease towards the rims. Despite five spots with a slightly positive Eu anomaly ( $\text{Eu}/\text{Eu}^* = 1.01$  to  $1.57$ ), the generally mild negative Eu anomaly ( $\text{Eu}/\text{Eu}^* = 0.59$  to  $0.98$ ) in this sample is interpreted as a response to the presence of plagioclase in the metamorphic assemblage. Garnet from this sample shows Lu enrichment in several growth zones of the crystal (Fig. 8b), whereas another analysed crystal (supplementary figures) shows a bell-shaped profile suggesting Lu partitioning into the core. Due to this non-uniform distribution of Lu in garnet crystals of this sample, we interpret the Lu-Hf garnet–WR age of  $563 \pm 1$  Ma as representing an average age of the garnet growth in sample MAB56A. Hf mean content acquired in LA–ICP–MS analyses ( $\sim 0.1$  ppm) differs from the value found after garnet isotope dilution (2.5 ppm) and may suggest that some ilmenite micro-inclusions were dissolved together with garnet. However, ilmenite is considered part of the stable mineral assemblage, together with garnet. As such, its presence as inclusion in the garnet crystals should not influence the resulting age estimate.

The peak *PT* condition reached during garnet growth was estimated at  $\sim 545$ – $565^\circ\text{C}$  and 4.3–5.3 kbar (Fig. 4). Even though garnet grains in the sample MAB56A are often relict crystals, our *PT* estimates are based primarily on the composition of garnet that largely escaped retrogressive dissolution (Fig. 3b). This evolution of the sample does not rule out potentially higher peak metamorphic conditions than indicated by the matrix mineral assemblage. Thus, staurolite crystals might have been present during the metamorphic peak, as suggested by the thermodynamic model (Fig. 4), and they could have been subsequently consumed during retrogression, while some garnet crystals remained preserved. Despite the potential discrepancy between the observed mineral assemblage and estimated metamorphic conditions, we interpret

the Lu-Hf garnet age ( $563 \pm 1$  Ma) and the *PT* conditions estimated from the garnet composition as reflecting/approaching the metamorphic peak in this region of the PC prior to the retrograde re-equilibration of sample MAB56A.

### **MAB56A - Retrogression in the northwestern Porongos Complex (ca. 540 Ma)**

Monazite in sample MAB56A appears in garnet cracks together with chlorite, and its growth thus appears temporally related to garnet chloritization (Fig. 9g, h). Such observation, together with garnet being mostly present as relict crystals, suggests retrograde reworking of the sample. Even though the dated monazite grains are approximately ten times bigger than those observed in the garnet cracks, their homogeneous U–Pb isotopic composition does not suggest multiple monazite-forming/modifying events, and we thus associate the monazite age of  $541 \pm 7$  Ma with the garnet breakdown. Such interpretation is also supported by the ~20 m.y. difference between the garnet and monazite age. Their respective ages (including  $2\sigma$  errors) do not overlap, which provides strong evidence that the growth or isotopic modification of the large monazite grains is not connected with garnet growth. Monazite grains display a strong variation in HREE content. However, colour-coded REE curves and corresponding dates in the U–Pb concordia diagram (Fig 9c, d) show that the variation in HREE content is not reflected in the U–Pb date of the analysed grains, as they all overlap and form a homogeneous cluster in the concordia diagram. Such results suggest that all dated grains represent the same monazite-growing/modifying event. The Th/U ratios of the analysed crystals are similar and thus support this interpretation. In this sample, garnet cores are systematically richer in HREE than their rims (Fig. 9a). We thus interpret the variation of monazite HREE content as related to the position of the monazite grain during its growth with respect to the garnet, i.e., monazites grains found in garnet-core cracks are richer in HREE, than those found in the cracks of garnet rims. The calculation with *Perple\_X* predicts ca. 6 vol.% of garnet at the peak metamorphic conditions, whereas its mode decreases to ca. 3 vol.% in the stability field of the observed retrograde mineral assemblage, which is in accord with the estimate from the thin section.

An alternative interpretation by Hagen-Peter et al. (2016) suggests a time-related coupling of garnet breakdown and monazite growth. In such a case, the older monazite grains would be HREE depleted, as they would have grown from garnet rims, whereas the younger monazites related to the dissolution of garnet cores would be richer in HREE. Although this interpretation cannot be fully discarded, the resolution of our dating is not high enough to determine a relationship between age and HREE content. Another alternative proposed by Hacker et al. (2019) suggests that temperature elevation caused by a heating event could raise the partitioning

coefficient of HREE into monazite, allowing new grains to support a larger amount of HREE in their structure. The spatially and temporally nearest intrusion is the Capané metagranite, which, according to Zvirtes et al. (2017), crystallized at  $603 \pm 6$  Ma (U–Pb zircon age – LA–ICP–MS) and has a metamorphic age of  $539 \pm 9$  Ma (U–Pb age from zircon rims and titanite age – LA–ICP–MS). Such data indicate that the intrusion is too old to provide heat at ca. 540 Ma. On the other hand, the metamorphic age of the Capané metagranite is in accord with the monazite age of the metasedimentary sample MAB56A.

The Eu anomalies in MAB56A monazite and garnet are similar ( $\text{Eu}/\text{Eu}^*_{\text{mon}} = 0.36$  to  $0.63$ ;  $\text{Eu}/\text{Eu}^*_{\text{grt}} = 0.59$  to  $1.56$ ). Also, distribution coefficients between monazite and garnet for some REEs (La–Tb; Fig. 10c, d) follow the expected equilibrium values from previous studies (Hermann and Rubatto 2003; Rubatto et al. 2006), although petrographic observations attest to disequilibrium between these minerals (Fig. 9g, h). On the other hand, Kd curves for the HREE suggest equilibrium only in a few cases, and most of the HREE Kd curves for monazite/garnet core and garnet mantle deviate from expected equilibrium values (Fig. 10c, d). The HREE Kd values for monazite/garnet rim show a large spread (up to three orders of magnitude) for each element, where some of the values match the expected equilibrium values, some are higher, and some are lower (Fig. 10c, d). This reflects the strongly variable HREE content of the monazite itself (Fig. 9b), and as mentioned above, we interpret this feature as a result of the variable availability of HREEs during monazite growth, which will largely depend on the distance of the growing monazite from the dissolving garnet, as well as on the particular part of the garnet (core, mantle, rim) releasing the HREEs.

Thus, we interpret the monazite U–Pb SIMS concordia age of  $541 \pm 7$  Ma ( $2\sigma$ ) as the time of retrograde overprint of sample MAB56A.

### **BD03 – Prograde metamorphism in the Passo Feio Complex (ca. 570 Ma)**

The garnet Lu–Hf dating of sample BD03 yielded an age of  $571 \pm 2$  Ma. In agreement with previous works (Bitencourt 1983; Costa et al. 2021), we interpret the garnet in this sample as syn-kinematic to the main progressive deformational-metamorphic event in the complex, represented by the main schistosity. Therefore, the ca. 570 Ma age is interpreted as the mean age of the prograde metamorphism of the Passo Feio Complex. Also, as Lu is not concentrated within one growth zone of the garnet (Fig. 8c), the Lu–Hf garnet–WR dating result is considered an average age of the garnet growth in sample BD03. The mean Hf content acquired by LA–ICP–MS (<1 ppm) presents a discrepancy when compared to the value found from garnet isotope dilution (4



ppm). However, as in sample MAB51B, all the garnet aliquots stay aligned in the isochron, and thus the same interpretation is applied to sample BD03, which indicates the age is likely trustful.

Thermodynamic modelling of sample BD03 places the peak metamorphic conditions of this event at ~560–580 °C and 4.7–6.4 kbar, with initial garnet growth at ~525–545 °C and 4.1–4.5 kbar. The data agree with the estimates of Costa et al. (2021) for a nearby sample of a garnet-staurolite schist, whereas their additional estimate for a staurolite-free garnet phyllite places the metamorphic peak to ~500–510 °C and 5–6.4 kbar (Table 4).

Published geochronological data for the main metamorphic event in the PFC are rather limited. A single SHRIMP spot in a zircon rim yielded a date of  $685 \pm 12$  Ma (Remus et al. 2000) that was associated with the metamorphic peak and thus contrasts with the  $571 \pm 2$  Ma Lu-Hf garnet age. However, the available image (Fig. 5i in Remus et al. 2000) suggests that the microprobe beam size was larger than the zircon rim width, which points to a possible mixed analysis with the Tonian (843 Ma) zircon core.

A second, low-pressure metamorphic event overprinted the peak mineral assemblage in the PFC (Bitencourt 1983; Costa et al. 2021), and it was interpreted as being related to the emplacement of the Caçapava Granite at  $562 \pm 8$  Ma (SHRIMP U–Pb zircon – Remus et al. 2000). The dextral transcurrent fabric generated in such second event cross-cuts the main metamorphic foliation (Costa et al. 2021). Thus, despite the overlap of the ages within their respective errors ( $M_1$  at  $571 \pm 2$  Ma and  $M_2$  at  $562 \pm 8$  Ma), metamorphic and structural field relations attest that  $M_1$  preceded the  $M_2$  event, or they are even progressive phases.

#### **INSERT TABLE 4**

### **Geological significance of the data and an evolutionary scenario for the Porongos and Passo Feio complexes**

The geochronological and metamorphic data presented in this work can be summarized in a  $P$ – $T$ – $t$  diagram showing the evolution and mutual relationships of Porongos and Passo Feio complexes (Fig. 11). The data show progressive thickening of the central Dom Feliciano foreland taking place in at least two distinct periods.

The early phase of orogenic evolution in the foreland is recorded by the prograde metamorphism of mica schists in the eastern region of the Porongos Complex. Estimates of metamorphic conditions by De Toni et al. (2021) and Lenz (2006) suggest a clockwise path for this region (see lines 1 and 2 in Fig. 11a). Garnet started to grow at ~ 555–565°C and 5.4–5.7 kbar and the metamorphic peak was reached at conditions of 560–580°C and 5.8–6.3 kbar



(MAB52A – De Toni et al. 2021). Such data demonstrate early thickening of the foreland crust with an apparent geothermal gradient ranging from 25 to 35°C/km at ca. 660 Ma (Fig. 11a – line 1), as demonstrated by the Lu-Hf garnet-WR age. For many authors (e.g. Saalman et al. 2006; Höfig et al. 2018; Battisti et al. 2018; De Toni et al. 2021), the main metamorphic–deformation event in the PC was related to the well-known collision in the DFB at ca. 650 Ma (Chemale et al. 2011; Martil 2016), which generated W-verging thrust of hinterland nappes on top of the foreland (Battisti et al. 2018; De Toni et al. 2021). Our Lu-Hf garnet–WR dating confirms the timing of the main fabric development and metamorphic peak in the eastern region of PC during this ca. 660–640 Ma event.

The post-exhumation evolution of the eastern Porongos Complex (Fig. 11a - line 2) is registered by the destabilization of the peak metamorphic assemblage and growth of andalusite crystals in the mica-schist samples (De Toni et al. 2021; Lenz 2006). Lenz (2006) estimated the conditions of this event at 550–560°C and 2.7 kbar. As discussed above, we associate these fluid-triggered mineralogical changes with the growth of monazite in sample MAB51B dated at ca. 615 Ma. All these data suggest that the eastern PC was exhumed between ca. 660 and 615 Ma, i.e. before the onset of extensive magmatic activity in the region at ca. 610 Ma.

The second phase of thickening of the foreland is recorded in the northwestern region of the Porongos Complex (line 3 in Fig. 11b) and in the Passo Feio Complex (lines 5 and 7 in Fig. 11c). The evolution of sample MAB56A from the northwestern Porongos Complex shows the onset of garnet growth at 520–540°C and 3.9–5.3 kbar and the metamorphic peak at ~545–565°C, and 4.3–5.3 kbar. Together with Lu-Hf garnet-WR dating, such data indicate a burial event at ca. 565 Ma. The exhumation of the PC northwestern region was associated with severe chloritization of the garnet-bearing peak mineral assemblage. It took place at around 540 Ma (Fig. 11b – line 4), as suggested by monazite growth at the expense of the ca. 565 Ma garnet. This second thickening event is exclusively recorded northwest of the Santana da Boa Vista thrust fault (Fig. 2).

Burial of the Passo Feio Complex took place at ca. 570 Ma (Fig. 11c – lines 5 and 7), as determined by Lu-Hf dating of garnet growth during the main regional metamorphism of the complex. Sample BD03 registers the metamorphic peak of this event at ~560–580 °C and 4.7–6.4 kbar. The exhumation of the complex occurred before ca. 560 Ma (Fig. 11c – line 6), which is the age of the Caçapava granite intrusion triggering contact metamorphism at depths shallower than 14 km, as indicated by the crystallization of andalusite (Costa et al. 2021). The exact exhumation path is unclear (line 6 in fig. 11c) and either corresponds to a near isothermal decompression path or to an exhumation and cooling path followed by re-heating (Costa et al. 2021), both due to the heat input caused by the Caçapava granite intrusion. *P–T* modelling also

indicates that andalusite is only stable at temperatures similar to those of the metamorphic peak but at lower pressures (Fig. 5).

## INSERT FIGURE 11

### Evolutionary model

Our geochronological and metamorphic data indicate a diachronous metamorphic evolution of the eastern and northwestern regions of the Porongos Complex. Such results explain the difference between these two regions, mainly noticed in the zircon provenance patterns of metasedimentary rocks (Gruber et al. 2011, 2016; Pertille et al. 2015b, 2015a, 2017; Höfig et al. 2018) and protolith ages of metaigneous rocks (Saalman et al. 2011; Pertille et al. 2017; Höfig et al. 2018; Battisti et al. 2022).

The older Porongos Complex sequence (called Cerro da Árvore after Jost and Bitencourt 1980; Fig. 2), and the Várzea do Capivarita Complex metasedimentary rocks (Fig. 2) have been deposited from before ca. 810 Ma, as indicated by the age of the associated volcanic rocks (Saalman et al. 2011; Pertille et al. 2017; Battisti et al. 2022), until ca. 660–640 Ma, when the early orogenic deformation and metamorphism took place (Fig. 12a). The ca. 660–640 Ma collisional event affected the easternmost part of the Cerro da Árvore sequence, which was thrust under the developing hinterland represented by the *W*-verging nappes of the Várzea do Capivarita Complex (Martil et al. 2017; Battisti et al. 2018; De Toni et al. 2021) but had minor effect on the westernmost part of this sequence (Fig. 12b). Sometime between ca. 660 Ma and ca. 615 Ma, the eastern PC was exhumed. The exhumation preceded an extensive magmatic activity in the region, during which at least some intrusions likely exploited the existing nappe boundaries. The ca. 660–640 Ma collisional event happened when the stretched crust of the Nico Pérez–Congo blocks, where the Várzea do Capivarita Complex and older sequence of the Porongos Complex originated, was inverted and thrust over its western border (Rio de la Plata Craton and São Gabriel arc – Fig. 12b).

In the PC western region, the basin with the pre-orogenic infill of the Cerro da Árvore sequence started receiving synorogenic (flysch) sediments of the present-day Porongos Complex Capané sequence. Based on the data of this study, the flysch sedimentation took place any time from ca. 660 Ma to ca. 570–560 Ma (Fig. 12b). At ca. 570–560 Ma, the second episode of crustal thickening occurred. The eastern region of PC was thrust on top of its western region, which caused metamorphism and deformation of both the Capané (younger) and Cerro da Árvore (older) PC sequences (Fig. 12c). The MAB56A locality represents the region where the Cerro da Árvore

and Capané sequences are interleaved. The destabilization of garnet and appearance of monazite in equilibrium with retrograde chlorite at ca. 540 Ma likely indicates the exhumation-related decrease of metamorphic temperatures from ca. 560 Ma to ca. 540 Ma.

Our new data suggest that the crustal thickening and overall tectonic activity in the central Dom Feliciano Belt foreland at ca. 570–560 Ma was much more extensive than so far published. Such data indicate that the Passo Feio and western Porongos complexes record an orogenic front migration towards the west as a part of a long-lived transpressive deformation in the Dom Feliciano Belt, which has started at ca. 660–640 Ma (see also De Toni et al. 2021; Percival et al. 2022, 2023).

## **INSERT FIGURE 12**

### **Connection with the African part of the orogenic system**

The metamorphic–deformation event at ca. 650 ( $\pm 10$ ) Ma is well documented in the hinterland domain of the Dom Feliciano–Kaoko–Gariép orogenic system. High-grade metamorphism of this age was registered in the central and southern sectors of the Dom Feliciano Belt in the Várzea do Capivarita (e.g. Battisti et al. 2022; Chemale et al. 2011; Martil et al. 2017) and Cerro Olivo (e.g. Gross et al. 2006, 2009; Oyhantçabal et al. 2009; Lenz et al. 2011; Basei et al. 2011; Peel et al. 2018; Will et al. 2019) complexes, as well as in the Coastal Terrane of the Kaoko Belt (Franz et al. 1999; Goscombe et al. 2005). Until recently, this timing of deformation was not recognized in the foreland regions of the orogenic system, which led several authors to interpret that the 650 ( $\pm 10$ ) Ma event is not connected with orogenic evolution but with the building of a magmatic arc above the subducting oceanic crust (e.g. Basei et al. 2000, 2018; Goscombe et al. 2005; Hueck et al. 2018).

The first interpretations that the ca. 650 ( $\pm 10$ ) Ma event may represent thrusting of the orogenic hinterland over the South American foreland domain were published by Battisti et al. (2018) and De Toni et al. (2021). These interpretations were later confirmed by a detailed petrochronological work in the northern Dom Feliciano Belt foreland by Percival et al. (2022). The petrochronological data presented in this paper demonstrate for the first time that the 650 ( $\pm 10$ ) Ma metamorphic–deformational episode is also registered in the foreland of the central sector of the Dom Feliciano Belt and thus confirm the earlier interpretation of Battisti et al. (2018). Furthermore, the data of Percival et al. (2022) and the new data presented in this work show that the 650 ( $\pm 10$ ) Ma thrusting event is registered along a large part of the Dom Feliciano Belt

hinterland–foreland boundary and confirm it as the main event that has shaped the regional architecture along the western edge of the orogenic system.

The main deformation event in the African Kaoko Belt occurred at 580–550 Ma when the Coastal Terrane was thrust over the eastern/southeastern Congo Craton margin (Goscombe et al. 2005; Konopásek et al. 2005, 2008; Goscombe and Gray 2007; Ulrich et al. 2011). The same timing for contractional evolution is known from the Gariep Belt, representing the southern African part of the orogenic system. There, inversion of the pre-orogenic Gariep basin started at ~ 580 Ma. The contractional period in the Gariep Belt lasted for ca. 35 My, and the belt reached its metamorphic peak at ca. 545 Ma (Frimmel and Frank 1998).

So far, the thrusting event in the Dom Feliciano Belt, corresponding to the 580–550 Ma crustal thickening on the African side of the orogenic system, has not been demonstrated. Our petrochronological data for the second crustal thickening episode in the Central Dom Feliciano belt presented in this paper suggest its close connection with the main deformation period in the Kaoko and Gariep belts. The Lu-Hf garnet ages of  $563 \pm 1$  and  $571 \pm 2$  Ma registered in the western Porongos and Passo Feio complexes, respectively, demonstrate for the first time that the crustal thickening event that shaped the African side of the orogenic system was also important in building the regional architecture of the central Dom Feliciano Belt foreland.

## CONCLUSIONS

A petrochronological study utilizing petrological modelling combined with Lu-Hf garnet–WR ages, U–Pb monazite SIMS ages and REE data in garnet and monazite was performed in metasedimentary rocks of the central Dom Feliciano Belt foreland. The results allow us to draw the following conclusions.

- 1) Metasedimentary rocks of the eastern Porongos Complex display a main metamorphic event at  $654 \pm 2$  Ma (Lu-Hf isochron garnet–whole-rock age). Such event took place at ~555–565 °C and 5.4–5.7 kbar and reached metamorphic peak at ~560–580 °C and 5.8–6.3 kbar. This episode represents an early orogenic thickening event in the foreland as a response to the beginning of the transpressive convergent evolution of the Dom Feliciano Belt.
- 2) The monazite age of  $614 \pm 6$  Ma (U–Pb SIMS) suggests that the eastern Porongos Complex was exhumed sometime between ca. 660 and 615 Ma. The growth of monazite, andalusite and secondary white mica was likely triggered by a release of fluids during the crystallisation of neighbouring syenitic rocks of similar age.

- 3) Syn-orogenic sediments (Capané sequence) were deposited in the western part of the Porongos Complex at an unspecified time between ca. 660 to ca. 560 Ma. This region's main metamorphic and deformational event occurred at  $\sim 545\text{--}565^\circ\text{C}$  and 4.3–5.3 kbar at  $563 \pm 1$  Ma (garnet-WR Lu-Hf isochron age).
- 4) The exhumation of western PC is dated by the appearance of monazite crystallised during garnet breakdown, suggesting retrograde metamorphism at  $541 \pm 7$  Ma (U-Pb SIMS).
- 5) The main metamorphic fabric in the Passo Feio Complex has developed at  $571 \pm 2$  Ma (garnet-WR Lu-Hf isochron age) at metamorphic conditions of  $\sim 560\text{--}580^\circ\text{C}$  and 4.7–6.4 kbar.
- 6) The Western part of the Porongos Complex and the Passo Feio Complex were deformed at ca. 570–565 Ma at similar *PT* conditions and geothermal gradients. These regions record a second crustal thickening event in the Dom Feliciano Belt and the orogenic front migration towards the west in a long-lived transpressive orogenic system.
- 7) The Lu-Hf garnet ages of  $563 \pm 1$  and  $571 \pm 2$  Ma registered in the western Porongos and Passo Feio complexes, respectively, demonstrate for the first time that the crustal thickening event that shaped the African side of the orogenic system was also important in building the regional architecture of the central Dom Feliciano Belt foreland.

## ACKNOWLEDGEMENTS

The authors acknowledge Coordenação de Aperfeiçoamento de Pessoal Docente for funding of the CAPES (Brazil) – Diku (Norway) cooperation program (CAPES - 88881.117872/2016-01 and 88887.141226/2017–00, Diku – UTF-2018-CAPES-Diku/10004). M.B. acknowledges the Brazilian National Research Council (CNPq) for his PhD scholarship. J.K. acknowledges financial support from the Czech Science Foundation, grant no. 18-24281S. J.S. was supported by the CAS institutional support RVO 67985831. Susan Drago, Denise Moreira Canarin and Pedro Sulzbach de Andrade are acknowledged for microprobe, lab work, and fieldwork assistance, respectively. We thank Martin Whitehouse and Heejin Jeon for their support while using the NordSIMS ion probe in Stockholm, which is operated under Swedish Research Council infrastructure grant 2021-00276 (this is a NordSIMS publication #749).

## Declaration of interests

The authors declare that they have no known competing financial interests or personal relationships that could have appeared to influence the work reported in this paper.

### **CRedit author statement**

**Matheus Ariel Battisti:** Conceptualization, Investigation, Formal analysis, Writing - Review & Editing. **Jiří Konopásek:** Conceptualization, Investigation, Formal analysis, Writing - Review & Editing, Resources, Supervision. **Maria de Fátima Bitencourt:** Conceptualization, Investigation, Review & Editing, Resources, Supervision. **Jiří Sláma:** Formal analysis, Methodology, Review & Editing. **Jack James Percival:** Investigation, Formal analysis, Review & Editing. **Giuseppe Betino De Toni:** Investigation, Formal analysis, Review & Editing. **Stephanie Carvalho da Silva:** Investigation, Formal analysis, Review & Editing. **Elisa Oliveira da Costa:** Investigation, Review & Editing. **Jakub Trubač:** Formal analysis, Methodology.

## REFERENCES

- Aleinikoff JN, Schenck, WS, Plank, MO, Srogi, LA, Fanning, CM, Kamo, SL, Bosbyshell, H (2006) Deciphering igneous and metamorphic events in high-grade rocks of the Wilmington complex, Delaware: Morphology, cathodoluminescence and backscattered electron zoning, and SHRIMP U-Pb geochronology of zircon and monazite. *Bull Geol Soc Am* 118, 39–64. <https://doi.org/10.1130/B25659.1>
- Anczkiewicz R, Platt JP, Thirlwall MF, Wakabayashi J (2004) Franciscan subduction off to a slow start: Evidence from high-precision Lu-Hf garnet ages on high grade-blocks. *Earth Planet Sci Lett* 225, 147–161 <https://doi.org/10.1016/j.epsl.2004.06.003>
- Arena KR, Hartmann LA, Lana C (2016) Evolution of Neoproterozoic ophiolites from the southern Brasiliano Orogen revealed by zircon U-Pb-Hf isotopes and geochemistry. *Precambrian Res* 285, 299–314. <https://doi.org/10.1016/j.precamres.2016.09.014>
- Arena KR, Hartmann LA, Lana C (2018) U–Pb–Hf isotopes and trace elements of metasomatic zircon delimit the evolution of neoproterozoic Capané ophiolite in the southern Brasiliano Orogen. *Int Geol Rev* 60, 911–928. <https://doi.org/10.1080/00206814.2017.1355269>
- Arena KR, Hartmann LA, Lana C (2017) Tonian emplacement of ophiolites in the southern Brasiliano Orogen delimited by U-Pb-Hf isotopes of zircon from metasomatites. *Gondwana Res* 49, 296–332. <https://doi.org/10.1016/j.gr.2017.05.018>
- Basei M, Siga O, Masquelin H, Harara O, Reis Neto J, Preciozzi F (2000) The Dom Feliciano belt (Brazil-Uruguay) and its foreland (Rio de la Plata Craton): framework, tectonic evolution and correlations with similar terranes of southwestern Africa, in: Cordani, U.G. (Ed.), *Tectonic Evolution of South America*. 31st International Geological Congress, Rio de Janeiro, Brazil, pp. 311–334.
- Basei MAS, Frimmel HE, Campos Neto MC, de Araujo CEG, de Castro NA, Passarelli CR. (2018) The Tectonic History of the Southern Adamastor Ocean Based on a Correlation of the Kaoko and Dom Feliciano Belts. pp. 63–85. [https://doi.org/10.1007/978-3-319-68920-3\\_3](https://doi.org/10.1007/978-3-319-68920-3_3)
- Basei MAS, Peel E, Sánchez Bettucci L, Preciozzi F, Nutman AP. (2011) The basement of the Punta del Este Terrane (Uruguay): an African Mesoproterozoic fragment at the eastern border of the South American Río de La Plata craton. *Int J Earth Sci* 100, 289–304. <https://doi.org/10.1007/s00531-010-0623-1>
- Battisti MA, Bitencourt MF, De Toni GB, Nardi LVS, Konopásek J (2018) Metavolcanic rocks and orthogneisses from Porongos and Várzea do Capivarita complexes: A case for identification of tectonic interleaving at different crustal levels from structural and geochemical data in southernmost Brazil. *J South Am Earth Sci* 88, 253–274. <https://doi.org/10.1016/j.jsames.2018.08.009>
- Battisti MA, Bitencourt MF, Florisbal LM, Nardi LVS, Ackerman L, Sláma J, Padilha DF. (2023) Unravelling major magmatic episodes from metamorphic sequences of the Dom Feliciano Belt central sector, southernmost Brazil – A comparative study of geochronology, elemental geochemistry, and Sr-Nd data. *Precambrian Res* 385. <https://doi.org/10.1016/j.precamres.2022.106951>
- Battisti MA, Bitencourt MF, Schmitt R S, Nardi LVS, Martil MMD, De Toni GB, Pimentel MM, Armstrong R., Konopásek J (2022) Reconstruction of a volcano-sedimentary environment shared by the Porongos and Várzea do Capivarita complexes at 790 Ma, Dom Feliciano Belt, southern Brazil. *Precambrian Res* 378, 106774. <https://doi.org/10.1016/j.precamres.2022.106774>
- Baxter EF, Caddick MJ, Dragovic B (2017) Garnet: A Rock-Forming Mineral Petrochronometer. *Rev Mineral Geochemistry* 83, 469–533. <https://doi.org/10.2138/rmg.2017.83.15>



- Baxter EF, Scherer EE (2013) Garnet Geochronology: Timekeeper of Tectonometamorphic Processes. *Elements* 9, 433–438. <https://doi.org/10.2113/gselements.9.6.433>
- Bea F, Pereira MD, Stroh A. (1994) Mineral/leucosome trace-element partitioning in a peraluminous migmatite (a laser ablation-ICP-MS study). *Chem Geol* 117, 291–312. [https://doi.org/10.1016/0009-2541\(94\)90133-3](https://doi.org/10.1016/0009-2541(94)90133-3)
- Bitencourt MF, Nardi LVS. (1993) Late- to Postcollisional Brasiliano Magmatism in Southernmost Brazil. *An Acad Bras Cienc* 65, 3–16.
- Bitencourt MF, Nardi LVS (2000) Tectonic setting and sources of magmatism related to the southern Brazilian shear belt. *Rev Bras Geociencias* 30, 184–187.
- Bitencourt MF, 1983. Metamorfitos da região de Caçapava do Sul, RS – Geologia e Relações com o Corpo Granítico. Atas do 1º Simpósio Sul-Brasileiro Geol 37–48.
- Bitencourt MF, Hartmann LA. (1984a) Geoquímica das Rochas anfibolíticas da região de Caçapava do Sul - RS - Parte 1: caracterização geológica e petrográfica, elementos maiores e menores. An DO XXXIII Congr Bras Geol 4266–4277.
- Bitencourt MF, Hartmann LA. (1984b) Reconhecimento geoquímico dos xistos magnesianos da região do Passo Feio, Caçapava do Sul - RS. Congr Bras Geol (33 1984 Rio Janeiro, RJ) Anais Rio Janeiro SBG, 1984.
- Bitencourt MF, Nardi LVS, Florisbal LM, Heaman LM, (2015). Geology, geochronology and petrogenesis of a Neoproterozoic, syntectonic sillimanite- muscovite-biotite granite from southernmost Brazil. B Abstr 8th Hutt Symposium Granites Relat Rocks 179.
- Boyton WV. (1984) Geochemistry of Rare Earth Elements: Meteorite studies, in: Henderson, P. (Ed.), *Rare Earth Element Geochemistry*. Elsevier, New York, p. 63.
- Chemale F. (2000) Evolução Geológica do Escudo Sul-rio-grandense, in: Holz, M., De Ros, L.F. (Eds.), *Geologia Do Rio Grande Do Sul*. Universidade Federal do Rio Grande do Sul, Porto Alegre, Brasil, pp. 13–52.
- Chemale F, Philipp RP, Dussin IA, Formoso MLL, Kawashita K, Bertotti AL. (2011) Lu–Hf and U–Pb age determination of Capivarita Anorthosite in the Dom Feliciano Belt, Brazil. *Precambrian Res* 186, 117–126. <https://doi.org/10.1016/j.precamres.2011.01.005>
- Chu NC, Taylor RN, Chavagnac V, Nesbitt RW, Boella RM, Milton JA, German CR, Bayon G, Burton K (2002) Hf isotope ratio analysis using multi-collector inductively coupled plasma mass spectrometry: an evaluation of isobaric interference corrections. *J Anal At Spectrom* 17, 1567–1574. <https://doi.org/10.1039/b206707b>
- Connolly JAD. (2009). The geodynamic equation of state: What and how. *Geochemistry, Geophys Geosystems* 10. <https://doi.org/10.1029/2009GC002540>
- Connolly JAD. (2005) Computation of phase equilibria by linear programming: A tool for geodynamic modeling and its application to subduction zone decarbonation. *Earth Planet Sci Lett* 236, 524–541. <https://doi.org/10.1016/j.epsl.2005.04.033>
- Costa AFU (1997) Teste e modelagem geofísica da estruturação das associações litotectônicas pré-cambrianas no Escudo Sul-Rio-Grandense. PhD Thesis. Universidade Federal do Rio Grande do Sul, Porto Alegre, Brasil.
- Costa EO, Bitencourt MF, Tennholm T, Konopásek J, de Franceschi Moita T (2021) P-T-D evolution of the southeast Passo Feio Complex and the meaning of the Caçapava Lineament, Dom Feliciano Belt, southernmost Brazil. *J South Am Earth Sci* 103465. <https://doi.org/10.1016/j.jsames.2021.103465>
- De Toni GB, Bitencourt MF, Konopásek J, Battisti MA, Costa EO, Savian JF. (2021) Autochthonous origin of the Encruzilhada Block, Dom Feliciano Belt, southern Brazil, based on aerogeophysics, image analysis and PT-paths. *J Geodyn* 144. <https://doi.org/10.1016/j.jog.2021.101825>
- De Toni GB, Bitencourt MF, Konopásek J, Martini A, Andrade PHS, Florisbal LM, Campos RS (2020a) Transpressive strain partitioning between the Major Gercino Shear Zone and the Tijucas Fold Belt, Dom Feliciano Belt, Santa Catarina,

- southern Brazil. *J Struct Geol* 104058. <https://doi.org/10.1016/j.jsg.2020.104058>
- De Toni GB, Bitencourt MF, Nardi LVS, Florisbal LM, Almeida BS, Geraldés M (2020b) Dom Feliciano Belt orogenic cycle tracked by its pre-collisional magmatism: the Tonian (ca. 800 Ma) Porto Belo Complex and its correlations in southern Brazil and Uruguay. *Precambrian Res* 105702. <https://doi.org/10.1016/j.precamres.2020.105702>
- Engi M (2017) Petrochronology Based on REE-Minerals: Monazite, Allanite, Xenotime, Apatite BT - Reviews in Mineralogy & Geochemistry. *Rev Mineral Geochemistry* 83, 365–418.
- Engi M, Lanari P, Kohn MJ (2017) Significant Ages - An Introduction to Petrochronology. *Petrochronology* 83, 1–12. <https://doi.org/10.1515/9783110561890-002>
- Fernandes LAD, Menegat R, Costa AFU, Koester E, Porcher CC, Tommasi A, Kraemer G, Ramgrab GE, Camozzato, E. (1995) Evolução Tectônica Do Cinturão Dom Feliciano No Escudo Sul-Rio-Grandense: Parte II - Uma Contribuição a Partir Das Assinaturas Geofísicas. *Rev Bras Geociências* 25, 375–384. <https://doi.org/10.25249/0375-7536.1995375384>
- Fernandes LAD, Tommazi A, Porcher CC (1992) Deformation patterns in the southern Brazilian branch of the Dom Feliciano Belt: A reappraisal. *J South Am Earth Sci* 5, 77–96.
- Fossen H, Cavalcante GCG, Pinheiro RVL, Archanjo CJ (2019) Deformation – Progressive or multiphase? *J Struct Geol* 125, 82–99. <https://doi.org/10.1016/j.jsg.2018.05.006>
- Fragoso-Cesar ARS, Figueiredo MCH, Soliani Jr E, Faccini UF (1986) O Batólito Pelotas (Proterozóico Superior/Eopaleozóico) no escudo do Rio Grande do Sul. XXXIV Congr Bras Geol 1321–1342.
- Franz L, Romer RL, Dingeldey DP (1999). Diachronous Pan-African granulite-facies metamorphism (650 Ma and 550 Ma) in the Kaoko belt, NW Namibia. *Eur J Mineral* 11, 167–180. <https://doi.org/10.1127/ejm/11/1/0167>
- Fraser G, Ellis D, Eggins S (1997). Zirconium abundance in granulite-facies minerals, with implications for zircon geochronology in high-grade rocks. *Geology* 25, 607–610. [https://doi.org/10.1130/0091-7613\(1997\)025<0607:ZAIGFM>2.3.CO;2](https://doi.org/10.1130/0091-7613(1997)025<0607:ZAIGFM>2.3.CO;2)
- Frimmel H, Frank W (1998) Neoproterozoic tectono-thermal evolution of the Gariiep Belt and its basement, Namibia and South Africa. *Precambrian Res* 90, 1–28. [https://doi.org/10.1016/S0301-9268\(98\)00029-1](https://doi.org/10.1016/S0301-9268(98)00029-1)
- Fuhrman ML, Lindsley DH (1988) Ternary-feldspar modeling and thermometry. *Am Mineral* 73, 201–215.
- Gahlan H, Azer M, Asimow P, Al-Kahtany K (2016) Late Ediacaran post-collisional A-type syenites with shoshonitic affinities, northern Arabian-Nubian Shield: a possible mantle-derived A-type magma. *Arab J Geosci* 9. <https://doi.org/10.1007/s12517-016-2629-x>
- Gasser D, Jeřábek P, Faber C, Stünitz H, Menegon L, Corfu F, Erambert M, Whitehouse MJ (2015) Behaviour of geochronometers and timing of metamorphic reactions during deformation at lower crustal conditions: phase equilibrium modelling and U-Pb dating of zircon, monazite, rutile and titanite from the Kalak Nappe Complex, northern Norway. *J Metamorph Geol* 33, 513–534. <https://doi.org/10.1111/jmg.12131>
- Goscombe B, Gray D, Armstrong R, Foster DA, Vogl J (2005) Event geochronology of the Pan-African Kaoko Belt, Namibia. *Precambrian Res* 140, 103.e1-103.e41. <https://doi.org/10.1016/j.precamres.2005.07.003>
- Goscombe B, Gray DR (2007) The Coastal Terrane of the Kaoko Belt, Namibia: Outboard arc-terrane and tectonic significance. *Precambrian Res* 155, 139–158. <https://doi.org/10.1016/j.precamres.2007.01.008>
- Goscombe BD, Gray DR (2008) Structure and strain variation at mid-crustal levels in a transpressional orogen: A review of Kaoko Belt structure and the character of West Gondwana amalgamation and dispersal. *Gondwana Res* 13, 45–85. <https://doi.org/10.1016/j.gr.2007.07.002>
- Gray DR, Foster DA, Meert JG, Goscombe BD, Armstrong R, Trouw RAJ, Passchier CW (2008) A Damara orogen perspective on the assembly of southwestern Gondwana. In: Pankhurst, R.J., Trouw, R.A.J., Brito Neves, B.B., de

- Wit, M.J. (eds) *West Gondwana: Pre-Cenozoic Correlations Across the South Atlantic Region*. Geological Society, London, Special Publications, 294, pp 257–278.
- Gregory TR, Bitencourt MF, Nardi LVS, Florisbal LM, Chemale F (2015). Geochronological data from TTG-type rock associations of the Arroio dos Ratos Complex and implications for crustal evolution of southernmost Brazil in Paleoproterozoic times. *J South Am Earth Sci* 57, 49–60. <https://doi.org/10.1016/j.jsames.2014.11.009>
- Gross AOMS, Porcher CC, Fernandes LAD, Koester E (2006) Neoproterozoic low-pressure/high-temperature collisional metamorphic evolution in the Varzea do Capivarita Metamorphic Suite, SE Brazil: Thermobarometric and Sm/Nd evidence. *Precambrian Res* 147, 41–64. <https://doi.org/10.1016/j.precamres.2006.02.001>
- Gross AOMS, Droop GTR, Porcher CC, Fernandes LAD (2009) Petrology and thermobarometry of mafic granulites and migmatites from the Chafalote Metamorphic Suite: New insights into the Neoproterozoic P–T evolution of the Uruguayan—Sul-Rio-Grandense shield. *Precambrian Res* 170, 157–174. <https://doi.org/10.1016/j.precamres.2009.01.011>
- Gruber L, Porcher CC, Koester E, Bertotti, AL, Lenz, C, Fernandes LAD, Remus, MVD (2016) Isotope geochemistry and geochronology of syn-depositional volcanism in Porongos Metamorphic Complex, Santana da Boa Vista antiform, Dom Feliciano Belt, Brazil: onset of an 800 ma continental arc. *J Sediment Environ* 1. <https://doi.org/10.12957/jse.2016.22722>
- Gruber L, Porcher CC, Lenz C, Fernandes, LAD (2011) Proveniência de metassedimentos das sequências arroio Areião, Cerro Cambará e quartzo milonitos no Complexo Metamórfico Porongos, Santana da Boa Vista, RS. *Pesqui em Geociencias* 38, 205–223.
- Hacker B, Kylander-Clark A, Holder R (2019) REE partitioning between monazite and garnet: Implications for petrochronology. *J Metamorph Geol* 37, 227–237. <https://doi.org/10.1111/jmg.12458>
- Hagen-Peter G, Cottle JM, Smit M, Cooper AF (2016) Coupled garnet Lu-Hf and monazite U-Pb geochronology constrain early convergent margin dynamics in the Ross orogen, Antarctica. *J Metamorph Geol* 34, 293–319. <https://doi.org/10.1111/jmg.12182>
- Hartmann LA, Leite JAD, Da Silva LC, Remus MVD, McNaughton NJ, Groves DI, Fletcher IR, Santos JOS, Vasconcellos MAZ (2000) Advances in SHRIMP geochronology and their impact on understanding the tectonic and metallogenic evolution of southern Brazil. *Aust J Earth Sci* 47, 829–844. <https://doi.org/10.1046/j.1440-0952.2000.00815.x>
- Hartmann LA, Santos, JOS, Leite JAD, Porcher CC, Mcnaughton NJ (2003) Metamorphic evolution and U-Pb zircon SHRIMP geochronology of the Belizário ultramafic amphibolite, Encantadas Complex, southernmost Brazil. *An Acad Bras Cienc* 75, 393–403. <https://doi.org/10.1590/S0001-37652003000300010>
- Hermann J, Rubatto D (2003) Relating zircon and monazite domains to garnet growth zones: Age and duration of granulite facies metamorphism in the Val Malenco lower crust. *J Metamorph Geol* 21, 833–852. <https://doi.org/10.1046/j.1525-1314.2003.00484.x>
- Hoerlle GS, Remus MVD, Dani N (2022) Metamafic dyke and sill swarms in the Dom Feliciano Belt: Insights for post-collisional strike-slip tectonics and fluid-assisted metamorphism. *Precambrian Res* 383, 106906. <https://doi.org/10.1016/j.precamres.2022.106906>
- Höfig DF, Marques JC, Basei MAS, Giusti RO, Kohlrausch C, Frantz JC (2018) Detrital zircon geochronology (U-Pb LA-ICP-MS) of syn-orogenic basins in SW Gondwana: New insights into the Cryogenian-Ediacaran of Porongos Complex, Dom Feliciano Belt, southern Brazil. *Precambrian Res* 306, 189–208. <https://doi.org/10.1016/j.precamres.2017.12.031>
- Holland TJB, Powell R (2011) An improved and extended internally consistent thermodynamic dataset for phases of petrological interest, involving a new equation of state for solids. *J Metamorph Geol* 29, 333–383. <https://doi.org/10.1111/j.1525-1314.2010.00923.x>

- Hueck M, Oriolo S, Basei MAS, Oyhantçabal P, Heller BM, Wemmer K, Siegesmund S (2022) . Archean to early Neoproterozoic crustal growth of the southern South American Platform and its wide-reaching “African” origins. *Precambrian Res* 369. <https://doi.org/10.1016/j.precamres.2021.106532>
- Hueck M, Oyhantçabal P, Philipp RP, Basei MAS, Siegesmund S (2018) The Dom Feliciano Belt in Southern Brazil and Uruguay. pp. 267–302. [https://doi.org/10.1007/978-3-319-68920-3\\_11](https://doi.org/10.1007/978-3-319-68920-3_11)
- Johnson TE, Clark C., Taylor RJM, Santosh M, Collins AS (2015) Prograde and retrograde growth of monazite in migmatites: An example from the Nagercoil Block, southern India. *Geosci Front* 6, 373–387. <https://doi.org/10.1016/j.gsf.2014.12.003>
- Jost H, Bitencourt MF (1980) Estratigrafia e tectônica de uma fração da Faixa de Dobramentos Tijucas no Rio Grande do Sul. *Acta Geol Leop* 11, 27–59.
- Jweda J, Bolge L, Class C, Goldstein SL (2016) High Precision Sr-Nd-Hf-Pb Isotopic Compositions of USGS Reference Material BCR-2. *Geostand Geoanalytical Res* 40, 101–115. <https://doi.org/10.1111/j.1751-908X.2015.00342.x>
- Kirkland CL, Whitehouse MJ, Slagstad T (2009) Fluid-assisted zircon and monazite growth within a shear zone: A case study from Finnmark, Arctic Norway. *Contrib to Mineral Petrol* 158, 637–657. <https://doi.org/10.1007/s00410-009-0401-x>
- Knijnik DB (2018) Geocronologia U-Pb e geoquímica isotópica Sr-Nd dos granitoides sintectônicos às zonas de cisalhamento transcorrentes Quitéria Serra do Erval e Dorsal de Canguçu, Rio Grande do Sul, Brasil. PhD Thesis. Universidade Federal do Rio Grande do Sul, Porto Alegre - RS. In: <http://hdl.handle.net/10183/182067>.
- Koester E, Porcher CC, Pimentel MM, Fernandes LAD, Vignol-Lelarge ML, Oliveira LD, Ramos RC (2016) Further evidence of 777 Ma subduction-related continental arc magmatism in Eastern Dom Feliciano Belt, southern Brazil: The Chácara das Pedras Orthogneiss. *J South Am Earth Sci* 68, 155–166. <https://doi.org/10.1016/j.jsames.2015.12.006>
- Kohn MJ (2017) Titanite Petrochronology. *Rev Mineral Geochemistry* 83, 419–441. <https://doi.org/10.2138/rmg.2017.83.13>
- Konopásek J, Anczkiewicz R, Jeřábek P, Corfu F, Žáčková E (2019) Chronology of the saxothuringian subduction in the west sudetes (Bohemian massif, Czech Republic and Poland). *J Geol Soc London* 176, 492–504. <https://doi.org/10.1144/jgs2018-173>
- Konopásek J, Cavalcante C, Fossen H, Janoušek V (2020) Adamastor – an ocean that never existed? *Earth-Science Rev* 205, 103201. <https://doi.org/10.1016/j.earscirev.2020.103201>
- Konopásek J, Janoušek V, Oyhantçabal P, Sláma J, Ulrich S (2018) Did the circum-Rodinia subduction trigger the Neoproterozoic rifting along the Congo–Kalahari Craton margin? *Int J Earth Sci* 107, 1859–1894. <https://doi.org/10.1007/s00531-017-1576-4>
- Konopásek J, Košler J, Tajčmanová L, Ulrich S, Kitt SL (2008) Neoproterozoic igneous complex emplaced along major tectonic boundary in the Kaoko Belt (NW Namibia): Ion probe and LA-ICP-MS dating of magmatic and metamorphic zircons. *J Geol Soc London* 165, 153–165. <https://doi.org/10.1144/0016-76492006-192>
- Konopásek J, Kröner S, Kitt SL, Passchier CW, Kröner A (2005) . Oblique collision and evolution of large-scale transcurrent shear zones in the Kaoko belt, NW Namibia. *Precambrian Res* 136, 139–157. <https://doi.org/10.1016/j.precamres.2004.10.005>
- Lanari P, Engi M (2017) Local Bulk Composition Effects on Metamorphic Mineral Assemblages. *Rev Mineral Geochemistry* 83, 55–102.
- Larsen RB (2002) The distribution of rare-earth elements in K-feldspar as an indicator of petrogenetic processes in granitic pegmatites: Examples from two pegmatite fields in southern Norway. *Can Mineral* 40, 137–151. <https://doi.org/10.2113/gscanmin.40.1.137>
- Lee D (1999) Hafnium Isotope Stratigraphy of Ferromanganese Crusts. *Science* (80- ) 285, 1052–1054.

<https://doi.org/10.1126/science.285.5430.1052>

- Leite JAD, Hartman LOA, McNaughton NJ, Chemale F (1998) SHRIMP U/Pb zircon geochronology of neoproterozoic juvenile and crustal-reworked terranes in southernmost Brazil. *Int Geol Rev* 40, 688–705. <https://doi.org/10.1080/00206819809465232>
- Leite JAD, Hartmann LA, Fernandes LAD, McNaughton NJ, Soliani Jr. Ê, Koester E, Santos JOS, Vasconcellos MAZ (2000) Zircon U–Pb SHRIMP dating of gneissic basement of the Dom Feliciano Belt, southernmost Brazil. *J South Am Earth Sci* 13, 739–750 [https://doi.org/10.1016/S0895-9811\(00\)00058-4](https://doi.org/10.1016/S0895-9811(00)00058-4)
- Lena LO, Pimentel MM, Philipp RP, Armstrong R, Sato K (2014) The evolution of the Neoproterozoic São Gabriel juvenile terrane, southern Brazil based on high spatial resolution U-Pb ages and  $\delta^{18}\text{O}$  data from detrital zircons. *Precambrian Res* 247, 126–138 <https://doi.org/10.1016/j.precamres.2014.03.010>
- Lenz C (2006) Evolução metamórfica dos metapelitos da Antiforme Serra dos Pedrosas: condições e idades do metamorfismo p 111. Master's Thesis. Universidade Federal do Rio Grande do Sul, Porto Alegre, Brasil In: <http://hdl.handle.net/10183/8520>.
- Lenz C, Fernandes LAD, McNaughton NJ, Porcher CC, Masquelin H (2011) U–Pb SHRIMP ages for the Cerro Bori Orthogneisses, Dom Feliciano Belt in Uruguay: Evidences of a ~800Ma magmatic and ~650Ma metamorphic event. *Precambrian Res* 185, 149–163 <https://doi.org/10.1016/j.precamres.2011.01.007>
- Lopes CG, Pimentel MM, Philipp RP, Gruber L, Armstrong R, Junges S (2015) Provenance of the Passo Feio Complex, Dom Feliciano Belt: Implications for the age of supracrustal rocks of the São Gabriel Arc, southern Brazil. *J South Am Earth Sci* 58, 9–17 <https://doi.org/10.1016/j.jsames.2014.11.004>
- Marques JC, Roisenberg A, Jost H, Frantz JC, Teixeira RS (2003) Geologia e geoquímica das rochas metaultramáficas da Antiforme Capané, suíte metamórfica Porongos, RS. *Rev Bras Geociências* 33, 83–94
- Martil MMD (2016) O magmatismo de arco continental pré-colisional (790 ma) e a reconstituição espaço-temporal do regime transpressivo (650 ma) no Complexo Várzea Do Capivarita, Sul da Província Mantiqueira. PhD Thesis. Universidade Federal do Rio Grande do Sul, Porto Alegre, Brasil In: <http://hdl.handle.net/10183/149194>.
- Martil MMD, Bitencourt M de F, Nardi LVS, Schmitt R da S, Weinberg R (2017) Pre-collisional, Tonian (ca. 790 Ma) continental arc magmatism in southern Mantiqueira Province, Brazil: Geochemical and isotopic constraints from the Várzea do Capivarita Complex. *Lithos* 274–275, 39–52 <https://doi.org/10.1016/j.lithos.2016.11.011>
- Nardi LVS, Bitencourt M de F (2007) Magmatismo Granítico e Evolução Crustal no Sul do Brasil. 50 anos Geol - Inst Geociências da Univ Fed do Rio Gd do Sul 1, 125–141
- Oliveira, CHE, Chemale F, Jelinek AR, Bicca MM, Philipp RP (2014) U-Pb and Lu-Hf isotopes applied to the evolution of the late to post-orogenic transtensional basins of the Dom Feliciano Belt, Brazil. *Precambrian Res* 246, 240–255 <https://doi.org/10.1016/j.precamres.2014.03.008>
- Oriolo S, Oyhantçabal P, Wemmer K, Heidelberg F, Pfänder J, Basei MAS, Hueck M, Hannich F, Sperner B, Siegesmund S (2016) Shear zone evolution and timing of deformation in the Neoproterozoic transpressional Dom Feliciano Belt, Uruguay. *J Struct Geol* 92, 59–78 <https://doi.org/10.1016/j.jsg.2016.09.010>
- Oriolo S, Oyhantçabal P, Wemmer K, Siegesmund S (2017) Contemporaneous assembly of Western Gondwana and final Rodinia break-up: Implications for the supercontinent cycle. *Geosci Front* 8, 1431–1445 <https://doi.org/10.1016/j.gsf.2017.01.009>
- Oyhantçabal P, Siegesmund S, Wemmer K, Presnyakov S, Layer P (2009) Geochronological constraints on the evolution of the southern Dom Feliciano Belt (Uruguay). *J Geol Soc London* 166, 1075–1084 <https://doi.org/10.1144/0016-76492008-122>
- Padilha DF, Bitencourt M de F, Nardi LVS, Florisbal LM, Reis C, Geraldés M, Almeida BS (2019) Sources and settings of



- Ediacaran post-collisional syenite-monzonite-diorite shoshonitic magmatism from southernmost Brazil. *Lithos* <https://doi.org/10.1016/j.lithos.2019.06.004>
- Paim PSG, Chemale Junior F, Wildner W (2014) Estágios Evolutivos Da Bacia Do Camaquã (Rs). *Ciência e Nat* 36, 183–193 <https://doi.org/10.5902/2179460X13748>
- Patchett PJ, Tatsumoto M (1980) Hafnium isotope variations in oceanic basalts. *Geophys Res Lett*
- Peel E, Sánchez L, Angelo M, Basei S (2018) Geology and geochronology of Paso del Dragón Complex (northeastern Uruguay): Implications on the evolution of the Dom Feliciano Belt (Western Gondwana). *J South Am Earth Sci* 85, 250–262 <https://doi.org/10.1016/j.jsames.2018.05.009>
- Percival JJ, Konopásek J, Anczkiewicz R, Ganerød M, Sláma J, Campos RS, Bitencourt MF (2022) Tectono-Metamorphic Evolution of the Northern Dom Feliciano Belt Foreland, Santa Catarina, Brazil: Implications for Models of Subduction-Driven Orogenesis. *Tectonics* 41 <https://doi.org/10.1029/2021TC007014>
- Percival JJ, Konopásek J, Eiesland R, Sláma J, de Campos RS, Battisti MA, Bitencourt M de F (2021) Pre-orogenic connection of the foreland domains of the Kaoko–Dom Feliciano–Gariép orogenic system. *Precambrian Res* 354, 106060 <https://doi.org/10.1016/j.precamres.2020.106060>
- Percival JJ, Konopásek J, Oyhantçabal P, Sláma J, Anczkiewicz R (2023) Garnet growth and mineral geochronology constrains the diachronous Neoproterozoic convergent evolution of the southern Dom Feliciano Belt, Uruguay. *J Metamorph Geol* Accepted f <https://doi.org/10.1002/jmg.12734>
- Pertille J, Hartmann LA, Philipp RP (2015a) Zircon U–Pb age constraints on the Paleoproterozoic sedimentary basement of the Ediacaran Porongos Group, Sul-Riograndense Shield, southern Brazil. *J South Am Earth Sci* 63, 334–345 <https://doi.org/10.1016/j.jsames.2015.08.005>
- Pertille J, Hartmann LA, Philipp RP, Petry TS, de Carvalho Lana C (2015b) Origin of the Ediacaran Porongos Group, Dom Feliciano Belt, southern Brazilian Shield, with emphasis on whole rock and detrital zircon geochemistry and U–Pb, Lu–Hf isotopes. *J South Am Earth Sci* 64, 69–93 <https://doi.org/10.1016/j.jsames.2015.09.001>
- Pertille J, Hartmann LA, Santos JOS, McNaughton NJ, Armstrong R (2017) Reconstructing the Cryogenian–Ediacaran evolution of the Porongos fold and thrust belt, Southern Brasiliano Orogen, based on Zircon U–Pb–Hf–O isotopes. *Int Geol Rev* 59, 1532–1560 <https://doi.org/10.1080/00206814.2017.1285257>
- Philipp RP, Machado R (2002) O magmatismo granítico Neoproterozóico do Batólito Pelotas no sul do Brasil: novos dados e revisão da geocronologia regional. *Rev Bras Geociencias* 32, 277–290
- Philipp RP, Bom FM, Pimentel MM, Junges SL, Zvirtes G (2016a) SHRIMP U–Pb age and high temperature conditions of the collisional metamorphism in the Várzea do Capivarita Complex: Implications for the origin of Pelotas Batholith, Dom Feliciano Belt, southern Brazil. *J South Am Earth Sci* 66, 196–207 <https://doi.org/10.1016/j.jsames.2015.11.008>
- Philipp RP, Lusa M, Nardi LVS (2008) Petrology of dioritic, tonalitic and trondhjemitic gneisses from Encantadas Complex, Santana da Boa Vista, southernmost Brazil: paleoproterozoic continental-arc magmatism. *An Acad Bras Cienc* 80, 735–748 <https://doi.org/10.1590/S0001-37652008000400013>
- Philipp RP, Pimentel MM, Basei MAS, Salvi M, De Lena LOF, Vedana LA, Gubert ML, Lopes CG, Laux JH, Camozzato E (2021) U–Pb detrital zircon dating applied to metavolcano-sedimentary complexes of the São Gabriel Terrane: New constraints on the evolution of the Dom Feliciano Belt. *J South Am Earth Sci* 110, 103409 <https://doi.org/10.1016/j.jsames.2021.103409>
- Philipp RP, Pimentel MM, Chemale Jr F (2016b) Tectonic evolution of the Dom Feliciano Belt in Southern Brazil: Geological relationships and U–Pb geochronology. *Brazilian J Geol* 46, 83–104 <https://doi.org/10.1590/2317-4889201620150016>
- Porada H (1979) The Damara–Ribeira orogen of the Pan-African–Brasiliano cycle in Namibia (southwest Africa) and Brazil as interpreted in terms of continental collision. *Tectonophysics* 57, 237–265

- Ramos VA, Cingolani C, Junior FC, Naipauer M, Rapalini A (2017) The Malvinas (Falkland) Islands revisited: The tectonic evolution of southern Gondwana based on U-Pb and Lu-Hf detrital zircon isotopes in the Paleozoic cover. *J South Am Earth Sci* 76, 320–345 <https://doi.org/10.1016/j.jsames.2016.12.013>
- Rapela CW, Fanning CM, Casquet C, Pankhurst RJ, Spalletti L, Poiré D, Baldo EG (2011) The Rio de la Plata craton and the adjoining Pan-African/brasiliano terranes: Their origins and incorporation into south-west Gondwana. *Gondwana Res* 20, 673–690 <https://doi.org/10.1016/j.gr.2011.05.001>
- Regis D, Warren CJ, Mottram CM, Roberts NMW (2016) Using monazite and zircon petrochronology to constrain the P–T evolution of the middle crust in the Bhutan Himalaya. *J Metamorph Geol* 34, 617–639 <https://doi.org/10.1111/jmg.12196>
- Remus MVD, Hartmann LA, McNaughton NJ, Groves DI, Fletcher IR (2000) The link between hydrothermal epigenetic copper mineralization and the Cacapava Granite of the Brasiliano cycle in southern Brazil. *J South Am Earth Sci* 13, 191–216 [https://doi.org/10.1016/S0895-9811\(00\)00017-1](https://doi.org/10.1016/S0895-9811(00)00017-1)
- Rivera CB (2016) Construção do maciço sienítico Piquiri (609 a 683 Ma) por colocação sucessiva de pulsos de magma ultrapotássico e shoshonítico sob extensão no Escudo sul-rio-grandense. PhD Thesis. Universidade Federal do Rio Grande do Sul, Porto Alegre, Brasil. In: <http://hdl.handle.net/10183/201719>.
- Rocha BC, Moraes R, Möller A, Cioffi CR, Jercinovic MJ (2017) Timing of anatexis and melt crystallization in the Socorro–Guaxupé Nappe, SE Brazil: Insights from trace element composition of zircon, monazite and garnet coupled to U–Pb geochronology. *Lithos* 277, 337–355 <https://doi.org/10.1016/j.lithos.2016.05.020>
- Rubatto D, Chakraborty S, Dasgupta S (2013) Timescales of crustal melting in the Higher Himalayan Crystallines (Sikkim, Eastern Himalaya) inferred from trace element-constrained monazite and zircon chronology. *Contrib to Mineral Petrol* 165, 349–372 <https://doi.org/10.1007/s00410-012-0812-y>
- Rubatto D, Hermann J, Buick IS (2006) Temperature and bulk composition control on the growth of monazite and zircon during low-pressure anatexis (Mount Stafford, Central Australia). *J Petrol* 47, 1973–1996 <https://doi.org/10.1093/petrology/egl033>
- Saalmann K, Gerdes A, Lahaye Y, Hartmann LA, Remus MVD, Läufer A (2011) Multiple accretion at the eastern margin of the Rio de la Plata craton: the prolonged Brasiliano orogeny in southernmost Brazil. *Int J Earth Sci* 100, 355–378 <https://doi.org/10.1007/s00531-010-0564-8>
- Saalmann K, Hartmann LA, Remus MVD (2005) Tectonic Evolution of Two Contrasting Schist Belts in Southernmost Brazil: A Plate Tectonic Model for the Brasiliano Orogeny. *Int Geol Rev* 47(12), 1234–1259 <https://doi.org/10.2747/0020-6814.47.12.1234>
- Saalmann K, Hartmann LA, Remus MVD (2007) The assembly of West Gondwana—The view from the Rio de la Plata craton, in: *Special Paper 423: The Evolution of the Rheic Ocean: From Avalonian-Cadomian Active Margin to Alleghenian-Variscan Collision*. Geological Society of America, pp. 1–26 [https://doi.org/10.1130/2007.2423\(01\)](https://doi.org/10.1130/2007.2423(01))
- Saalmann K, Remus MVD, Hartmann LA (2006) Structural evolution and tectonic setting of the Porongos belt, southern Brazil. *Geol Mag* 143, 59 <https://doi.org/10.1017/S0016756805001433>
- Sbaraini S, B Raposo MI, Bitencourt M de F, Rocha Tomé C (2020) Magnetic fabrics of the neoproterozoic piquiri syenite massif (Southernmost Brazil): Implications for 3D geometry and emplacement. *J Geodyn* 134, 101691
- Schaltegger U, Davies JHFL (2017) Petrochronology of Zircon and Baddeleyite in Igneous Rocks: Reconstructing Magmatic Processes at High Temporal Resolution. *Rev Mineral Geochemistry* 83, 297–328 (<https://doi.org/10.2138/rmg.2017.83.10>)
- Soret M, Larson KP, Cottle JM, Smit M, Johnson A, Shrestha S, Ali A, Faisal S (2019) Mesozoic to Cenozoic tectono-



- metamorphic history of the South Pamir–Hindu Kush (Chitral, NW Pakistan): Insights from phase equilibria modelling, and garnet–monazite petrochronology. *J Metamorph Geol* 37, 633–666 (<https://doi.org/10.1111/jmg.12479>)
- Stevens LM, Baldwin JA, Cottle JM, Kylander-Clark ARC (2015) Phase equilibria modelling and LASS monazite petrochronology: P-T-t constraints on the evolution of the Priest River core complex, northern Idaho. *J Metamorph Geol* 33, 385–411 (<https://doi.org/10.1111/jmg.12125>)
- Stuwe K (1997) Effective bulk composition changes due to cooling: a model predicting complexities in retrograde reaction textures. *Contrib to Mineral Petrol* 129, 43–52.
- Thirlwall MF, Anczkiewicz R (2004) Multidynamic isotope ratio analysis using MC–ICP–MS and the causes of secular drift in Hf, Nd and Pb isotope ratios. *Int J Mass Spectrom* 235, 59–81 (<https://doi.org/10.1016/j.ijms.2004.04.002>)
- Ulrich S, Konopásek J, Jeřábek P, Tajčmanová L (2011) Transposition of structures in the Neoproterozoic Kaoko Belt (NW Namibia) and their absolute timing. *Int J Earth Sci* 100, 415–429 (<https://doi.org/10.1007/s00531-010-0573-7>)
- Vieira DT, Koester E, Ramos RC, Porcher CC, D'Ávila Fernandes, LA (2020) SHRIMP U–Pb zircon ages for the synkinematic magmatism in the Dorsal de Canguçu Transcurrent Shear Zone, Dom Feliciano Belt (Brazil): Tectonic implications. *J South Am Earth Sci* 100, 102603 (<https://doi.org/10.1016/j.jsames.2020.102603>)
- Walczak K, Anczkiewicz R, Szczepański J, Rubatto D, Košler J (2017) Combined garnet and zircon geochronology of the ultra-high temperature metamorphism: Constraints on the rise of the Orlica–Śnieżnik Dome, NE Bohemian Massif, SW Poland. *Lithos* 292–293, 388–400 (<https://doi.org/10.1016/j.lithos.2017.09.013>)
- Warren CJ, Greenwood LV, Argles TW, Roberts NMW, Parrish RR, Harris NBW (2019) Garnet–monazite rare earth element relationships in sub-solidus Metapelites: A case study from Bhutan. *Geol Soc Spec Publ* 478, 145–166 (<https://doi.org/10.1144/SP478.1>)
- Werle M, Hartmann LA, Queiroga GN, Lana C, Pertille J, Michelin CRL, Remus MVD, Roberts MP, Castro MP, Leandro CG, Savian JF (2020) Oceanic crust and mantle evidence for the evolution of Tonian–Cryogenian ophiolites, southern Brasiliano Orogen. *Precambrian Res* 351, 105979 (<https://doi.org/10.1016/j.precamres.2020.105979>)
- White RW, Powell R, Holland TJB, Johnson TE, Green ECR (2014) New mineral activity–composition relations for thermodynamic calculations in metapelitic systems. *J Metamorph Geol* 32, 261–286 (<https://doi.org/10.1111/jmg.12071>)
- Will TM, Gaucher C, Ling XX, Li XH, Li QL, Frimmel HE (2019) Neoproterozoic magmatic and metamorphic events in the Cuchilla Dionisio Terrane, Uruguay, and possible correlations across the South Atlantic. *Precambrian Res* 320, 303–322 (<https://doi.org/10.1016/j.precamres.2018.11.004>)
- Yakymchuk C, Clark C, White RW (2017) Phase Relations, Reaction Sequences and Petrochronology. *Rev Mineral Geochemistry* 83, 13–53 (<https://doi.org/10.2138/rmg.2017.83.2>)
- Zvirtes G, Philipp RP, Camozzato E, Guadagnin F (2017) Análise estrutural do Metagranito Capané, Complexo Porongos, Cachoeira do Sul, RS. *Pesqui em Geociências* 44, 05 (<https://doi.org/10.22456/1807-9806.78250>)

**Supplementary files content description:**

**File 1: Supplementary figures**

**File 2: Mineral chemistry data**

**File 3: Garnet and monazite trace-element data**

**File 4: Monazite U-Pb results**

**File 5: Monazite/garnet trace-element partitioning**

## Appendix

### 1. Lu-Hf isotope analysis

The Lu–Hf analyses were conducted at the Geological Institute of the Czech Academy of Sciences (chemistry) and Faculty of Science, Charles University (MC–ICP–MS). Garnet concentrates and whole-rock powders were weighted and mixed with the  $^{176}\text{Lu}$ – $^{180}\text{Hf}$  tracer solution. The samples were digested in closed 30ml Savillex Teflon vials using combined acid attack (HF– $\text{HNO}_3$ –HCl). First, 0.5 ml  $\text{HNO}_3$  + 2 ml HF (concentrated acids) was added to each sample and left to stand cold in a closed vial for 3 hours. Subsequently, the bombs were opened and warmed on the hotplate to 90 °C to evaporate Si and all acids. During this step, the major minerals are attacked by the acids, most of the Si evaporates with the excess HF, and the acids used in the following step thus can attack any resistant minerals without being depleted by reaction with major silicate phases. After complete evaporation, the mixture of 1.5 ml  $\text{HNO}_3$  + 4.5 ml HF was added to the samples, left on a hotplate for two days at 160 °C, and then evaporated to dryness. After that, the samples were treated three times with 2 ml of concentrated  $\text{HNO}_3$  and evaporated to dryness. Next, 1 ml of 6 M HCl was added and immediately dried down. Finally, 8 ml of 6 M HCl was added and left on a hotplate at 160 °C in a sealed beaker for 24 hours. The sample was then evaporated to dryness, and 2 ml of 1 M HCl was added for subsequent column chemistry.

The ion exchange column chemistry follows closely that of Anczkiewicz et al. (2004), which is a down-scale modification of the original setup of Patchett and Tatsumoto (1980). The separation of Hf (+ Ti) and Lu (+ Yb and LREE) fractions is first carried out on a standard cation exchange column using AG50W–X8 resin (200–400 mesh size) and 1 M HCl–0.06 M HF (HFSE elution) and 2.5 M HCl (REE elution). The final purification of Hf from other HFSE and potentially interfering Lu and Yb takes place on a second column with Eichrom LN resin (50–100  $\mu\text{m}$ ) using a technique based on Lee (1999) employing the mixture of 2 M HCl–0.1 M HF. The same column is then used to purify Lu from other REEs and reduce Yb in the Lu cut using 4M HCl.

All measurements of Lu and Hf fractions were carried out using a THERMO Neptune multi-collector (MC) ICP–MS in the labs of the Faculty of Science, Charles University in Prague. Hafnium isotopic compositions were analysed in a static mode using Faraday cups with the following configuration: L4 –  $^{172}\text{Yb}$ , L3 –  $^{174}\text{Yb}$ , L2 –  $^{175}\text{Lu}$ , L1 –  $^{176}\text{Hf}$ , C –  $^{177}\text{Hf}$ , H1 –  $^{178}\text{Hf}$ , H2 –  $^{179}\text{Hf}$ , H3 –  $^{180}\text{Hf}$ , H4 –  $^{182}\text{W}$ . Samples were aspirated to the instrument in 0.5 M  $\text{HNO}_3$ –0.25 M HF mixture using CETAC Aridus II desolvating nebulizer. The data acquisition procedure consisted of 40 integration cycles acquired over a period of ~ 6 min, followed by ~ 5 min of washout with a

mixture of 1.2 M HNO<sub>3</sub>–0.5 M HF composition. The raw data were processed offline using an on-purpose-built calculation EXCEL spreadsheet. Repeated measurements of 50 ppb JMC–475 standards throughout analyses yield  $^{176}\text{Hf}/^{177}\text{Hf} = 0.282158 \pm 7$  (2SE, n=7), which is in agreement within error with the reference data (Chu et al., 2002). The spike stripping routine employing the ratio of  $^{179}\text{Hf}/^{177}\text{Hf}$  iteratively deconvoluting to the natural value of 0.7325 (Patchett and Tatsumoto, 1980) and exponential mass-bias correction were used to obtain Hf isotopic composition and Hf concentration of the spiked samples.

For Lu isotopic analyses, Faraday cup configuration was as follows: L3 –  $^{171}\text{Yb}$ , L2 –  $^{172}\text{Yb}$ , L1 –  $^{173}\text{Yb}$ , C –  $^{174}\text{Yb}$ , H1 –  $^{175}\text{Lu}$ , H2 –  $^{176}\text{Lu}$ , H3 –  $^{177}\text{Hf}$ . The sample aspiration was identical to the Hf measurements, with the difference that HF-free acids were used for sample introduction (0.5 M HNO<sub>3</sub>) and washout (1.5 M HNO<sub>3</sub>). The data acquisition procedure consisted of 40 integration cycles acquired over a period of ~ 3 minutes, followed by 4 min of washout. The raw data were processed offline using an on-purpose-built calculation EXCEL spreadsheet. Repeated measurements of natural Lu and Yb standard solutions were carried out to check the accuracy of the isotopic ratio measurements. The mass-bias correction (exponential law) of the spiked  $^{176}\text{Lu}/^{175}\text{Lu}$  ratio was done using the natural Yb present in the sample (reduced in the 3<sup>rd</sup> step of column chromatography to be ~ 1/10 of the amount of Lu to be suitable for mass bias correction while not causing excessive interference on  $^{176}\text{Lu}$  mass) and the true ratio of  $^{174}\text{Yb}/^{172}\text{Yb} = 1.45198$  (Thirlwall and Anczkiewicz, 2004). The value of  $^{176}\text{Lu}/^{175}\text{Lu}$  was then used to calculate the concentration of Lu in the samples. The accuracy of the method was checked by measurement of spiked aliquot of BCR–2 reference material, which gave  $^{176}\text{Hf}/^{177}\text{Hf} = 0.282859 \pm 11$ , Hf = 5.00 ppm and Lu = 0.514 ppm, which are in good agreement with published values of  $0.282866 \pm 11$  (Jweda et al., 2016),  $4.8 \pm 0.2$  and  $0.51 \pm 0.02$  (U.S. Geological Survey Certificate of Analysis, online source) respectively.

## 2. U–Pb monazite dating methodology

The samples were processed through a rock crusher and a hammer mill. Monazite and garnet were separated using a Wilfley table, a Frantz™ isodynamic magnetic separator and heavy liquids in the laboratories of the Department of Geosciences at the UiT The Arctic University of Norway in Tromsø. Subsequently, monazite grains were handpicked under a binocular microscope, and selected grains were mounted in one-inch epoxy disks. In order to identify internal microstructures and possible compositional zoning, backscattered electron (BSE) images of monazite grains were made by Zeiss Merlin Scanning Electron Microscope (SEM) housed at the Faculty of Health Sciences of the same university.

Monazite U–Th–Pb analyses by SIMS were performed on a Cameca IMS 1280 ion probe at NordSIMS laboratory hosted by the Swedish Museum of Natural History in Stockholm. Operating parameters concerning primary beam and mass resolution were similar to those used for zircon, broadly following the protocols described (Gasser et al., 2015). The principal difference from zircon is that the monazite analyses employed both a smaller entrance slit (30  $\mu\text{m}$  instead of 75  $\mu\text{m}$ ) to limit the secondary beam intensity, as well as a smaller energy slit (30 eV instead of 45 eV) together with a -30 eV energy offset (applied via sample high voltage) on all the Pb,  $\text{ThO}_x$  and  $\text{UO}_x$  (where  $x = 0, 1$  or  $2$ ) peaks of interest to minimize matrix differences in potentially chemically diverse monazite and eliminate a small  $\text{ThNdO}_2^{2+}$  interference on  $^{204}\text{Pb}$  identified in earlier monazite studies (e.g. Kirkland et al., 2009). Secondary beam centring and optimization steps were performed as for zircon but using the  $\text{CePO}_2^+$  matrix peak at nominal mass 203. U–Pb ratios were calibrated against a 425 Ma reference monazite from a metapelite of the Wilmington Complex, Delaware (sample 44069, Aleinikoff et al., 2006), using a two-dimensional power law calibration approach, i.e.  $(\text{Pb}/\text{U})_{\text{true}} = f.(\text{Pb}/\text{U})_{\text{meas}}, \text{UO}_2/\text{U}_{\text{meas}}$  based on measurement of these ratios in the reference monazite.

## FIGURE CAPTIONS

Figure 1. **a** Overview geological map and main tectonic domains of the Dom Feliciano–Kaoko–Gariiep orogenic system (modified after Konopásek et al., 2018 and Bitencourt and Nardi, 2000). **b** Relative position of Africa and South America is shown at 140 Ma - after Heine et al., 2013. **c** Dom Feliciano Belt domains in the Rio Grande do Sul state are shown in the inset. Location of figure 2 is indicated. Cities: FL – Florianópolis, PA – Porto Alegre, MV – Montevideo, LÜ – Lüderitz, SW – Swakopmund.

Figure 2. Geological map of the studied area with the sampled sites indicated. DCZS – Dorsal do Canguçu Shear Zone; PCSZ – Passo das Canas Shear Zone. Tectonic division shown in the inset (*sensu* De Toni et al. (2021). References: 1 – Paim et al. (2014); 2 – Padilha et al. (2019); 3 – Rivera (2016), Padilha et al. (2019); 4 – Bitencourt et al. (2015), Knijnik (2018), Vieira et al. (2020); 5 – Knijnik (2018), Vieira et al. (2020); 6 – Remus et al. (2000); 7 – This paper; 8 – Battisti et al. (2023); 9 – Höfig et al. (2018); 10 – Philipp et al. (2016b); 11 – Saalman et al. (2011), Pertille et al. (2017), Battisti et al. (2022); 12 – Martil et al. (2017), Battisti et al. (2022); 13 – Gross et al. (2006), Chemale et al. (2011), Philipp et al. (2016a), Martil et al. (2017); 14 – Chemale et al. (2011); 15 – Leite et al. (2000), Hartmann et al. (2003), Saalman et al. (2011), Gregory et al. (2015).

Figure 3. **a** General view of MAB56A garnet-bearing plagioclase–biotite–quartz–muscovite schist. microstructure with detail of a relic of strongly dissolved garnet crystal. **b** Snowball garnet in MAB56A sample. **c** General view of BD03 muscovite–garnet–staurolite–biotite–plagioclase–quartz schist microstructure; **d** Detail of a garnet porphyroblast. **e** General view of MAB51B garnet–plagioclase–biotite–muscovite schist. The lower left inset shows a BSE image of the relationship between a relic of staurolite and monazite. **f** MAB52A staurolite-garnet-biotite-muscovite schist studied by De Toni et al. (2021) (30.74621° S, 52.81647 °W) from the same lithological unit as MAB51B. Photomicrographs were taken in plane-polarized (PPL) and cross-polarized light (XPL) to highlight the textural aspects of the rock. The lower left inset shows a pseudomorphic replacement of staurolite crystal by muscovite in the sample MAB52A.

Figure 4. *P–T* pseudosections calculated for sample MAB56A. **a** Phase diagram calculated for the bulk chemistry of the sample, showing conditions for the early garnet growth (pink polygon) and for the garnet rim stability (blue polygon). **b** Phase diagram calculated for the bulk rock chemistry modified by gradually removing corresponding garnet volume and composition along the selected fractionation path.



Figure 5. Calculated  $P$ – $T$  pseudosections for the sample BD03. **a** Phase diagram calculated for the bulk chemistry of the sample. **b** Phase diagram calculated for the bulk rock chemistry modified by gradually removing corresponding garnet volume and composition along the selected fractionation path. Although the  $P$ – $T$  conditions of stabilization of the matrix mineral assemblage are similar in both diagrams, the  $P$ – $T$  diagram for fractionated bulk rock composition shows a better match of the mineral composition with the peak metamorphic assemblage field (field 23 in **(a)**, and field 19 in **(b)**).

Figure 6. Results of the garnet–whole-rock Lu–Hf dating. Porongos Complex – sample MAB51B **(a)** and, sample MAB56A **(b)**, and Passo Feio Complex – sample BD03 **(c)**.

Figure 7. REE data for garnet **(a)** and monazite **(b)** in sample MAB51B, normalized to chondrite (Boyton, 1984). In **(a)**, colour coding of the REE curves indicates the distance of each analytical spot from the garnet centre. **c** BSE images showing textures of analysed monazite grains and their respective  $U^{238}/Pb^{206}$  dates. **d** U–Pb SIMS, concordia age of monazite, calculated from all analysed grains. In **(b)** and **(d)**, colour-coded REE curves and ellipses distinguish each SIMS spot in monazite grains shown in **(c)**. Textural relationships of monazite with other mineral phases in the thin section are illustrated in BSE images in **(e)**, **(f)** and **(g)**. Additional trace element data and garnet laser spots are presented as supplementary material.

Figure 8. Lu–Hf–U–Ti–Nd distribution curves for garnet of MAB51B **(a – grt1)** and MAB56A **(b – grt3)** – Porongos Complex; and garnet of BD03 **(c – grt5)** – Passo Feio Complex. The coloured bars indicate the presence of inclusions.

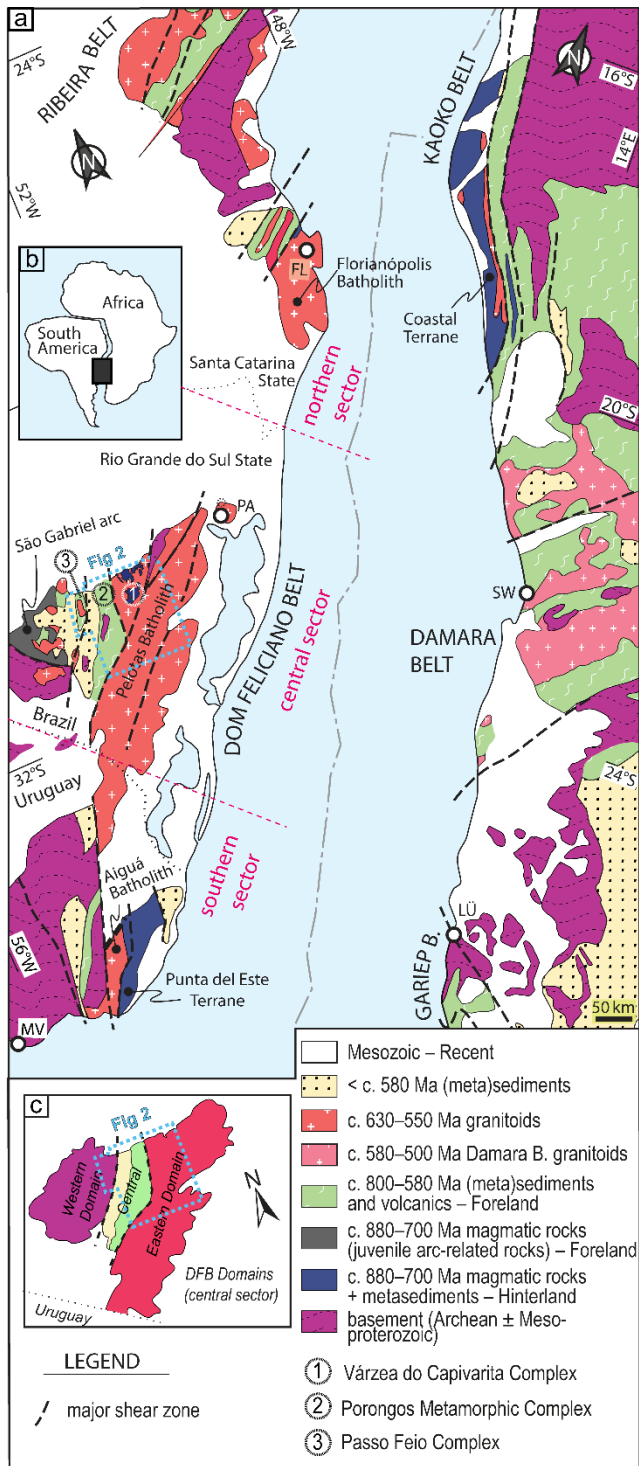
Figure 9. REE data for garnet **(a)** and monazite **(b)** in sample MAB56A), normalized to chondrite (Boyton, 1984). In **(a)**, colour coding of the REE curves indicates the distance of each analytical spot from the garnet centre. **c** BSE images showing textures of analysed monazite grains and their respective  $U^{238}/Pb^{206}$  dates. **d** U–Pb SIMS, concordia age of monazite, calculated from all analysed spots. In **(b)** and **(d)**, colour-coded REE curves and ellipses distinguish each SIMS spot in monazite grains shown in **(c)**. Textural relationships of monazite with other mineral phases in the thin section are illustrated in BSE images in **(e–h)**. Additional trace element data and garnet laser spots are presented as supplementary material.

Figure 10. Calculated distribution coefficients of REE between **a** monazite and garnet 1 and **b** monazite and garnet 2 in sample MAB51B and **c** monazite and garnet 3 and **d** monazite and garnet 4 in sample

MAB 56A. Dashed black lines: Mnz/Grt core, grey lines: Mnz/Grt mantle, dashed blue lines: Mnz/Grt rim.

Figure 11. P–T–t evolution of Eastern **(a)** and Northwestern **(b)** region of the Porongos and **(c)** Passo Feio complexes, based on the data of this paper and literature (see text for related references). **d** summary of the evolution of the studied complexes. Depth was calculated using average crustal density of 2.8 g/cm<sup>3</sup>.

Figure 12 – A pre-orogenic setting and two-stage orogenic evolution model of the Central Dom Feliciano Belt foreland (Porongos and Passo Feio complexes) and hinterland (Várzea do Capivarita Complex). **A)** Pre-orogenic evolution of the area showing the stage of continental stretching (ca. 800–770 Ma) and formation of extensional basins as precursors to the foreland and hinterland domains. **B)** Initial stage of orogenic evolution at ca. 660–640 Ma showing thrusting of the hinterland (Várzea do Capivarita Complex) over the volcano-sedimentary cover of the foreland (represented largely by the Cerro da Árvore sequence of the Porongos Complex). During this orogenic episode, the developing topography was gradually eroded and deposited as the early orogenic flysch deposits, which are the precursor of the Capané sequence in the western region of the Porongos Complex. **c** Second stage of orogenic evolution at ca. 570–560 Ma. The pre-orogenic sediments distal from the orogenic front and the early orogenic flysch sediments are involved in the second episode of crustal thickening in the foreland. This period is responsible for the metamorphism of the Capané sequence and the Passo Feio Complex. During this episode, the Cerro da Árvore and Capané sequences became tectonically interleaved in the northwestern region of the Porongos Complex.



**Figure 1**

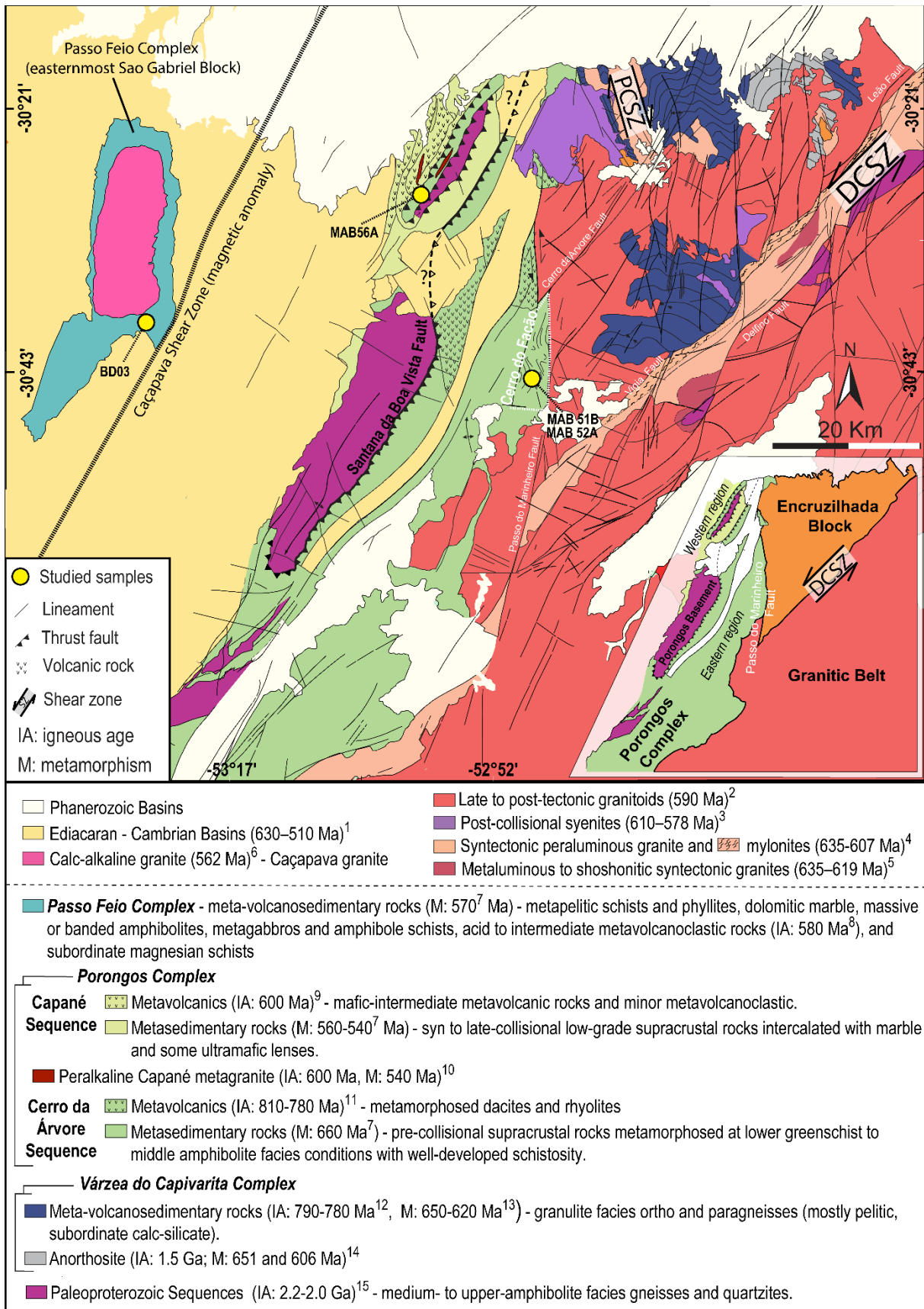
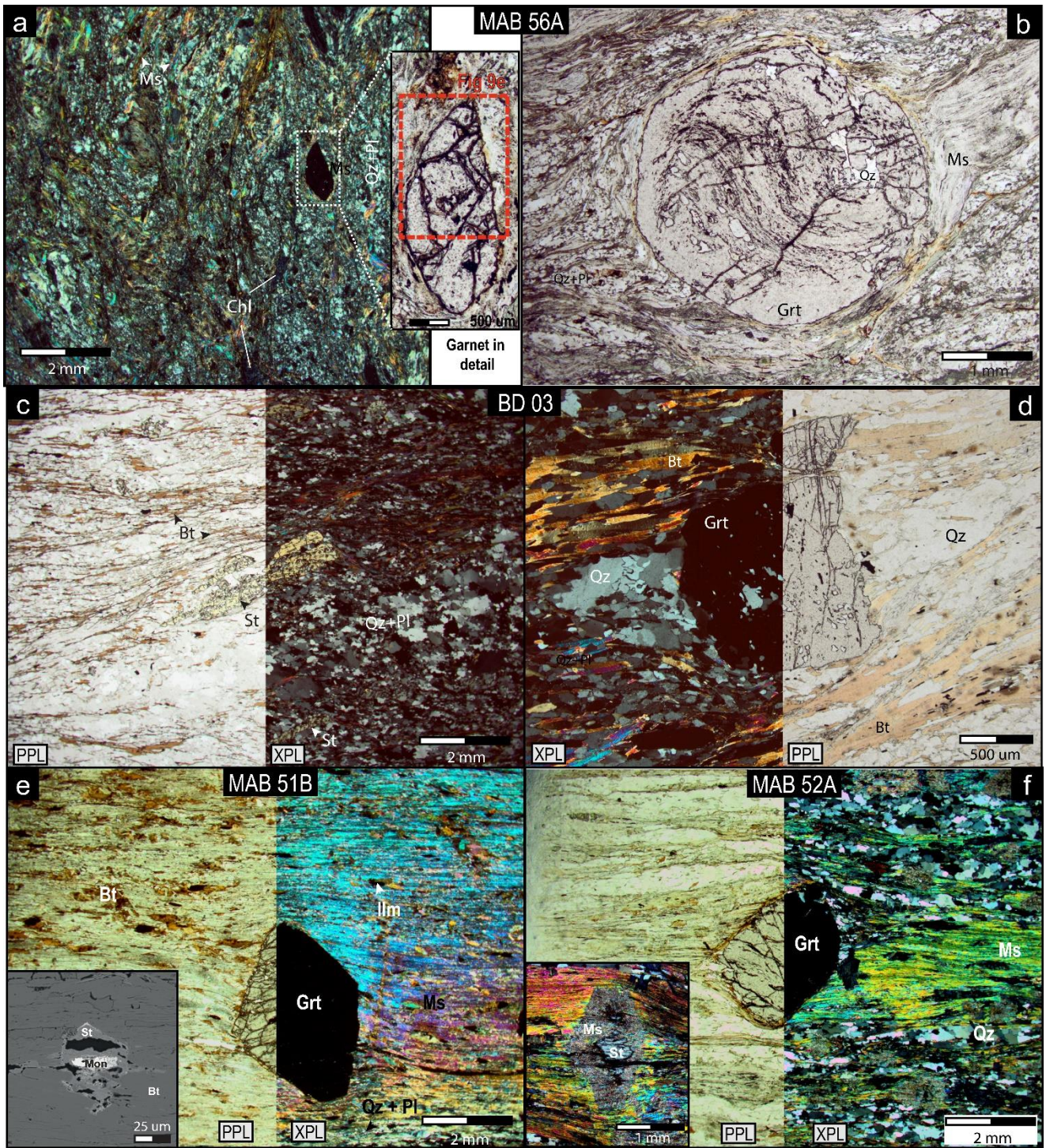


Figure 2





**Figure 3**







BD 03

Whole Rock  
Chemistry (wt%)

SiO<sub>2</sub> – 64.13 Al<sub>2</sub>O<sub>3</sub> – 15.61 TiO<sub>2</sub> – 0.96 FeO – 7.95 MnO – 0.12  
MgO – 3.13 CaO – 1.53 Na<sub>2</sub>O – 1.81 K<sub>2</sub>O – 2.60

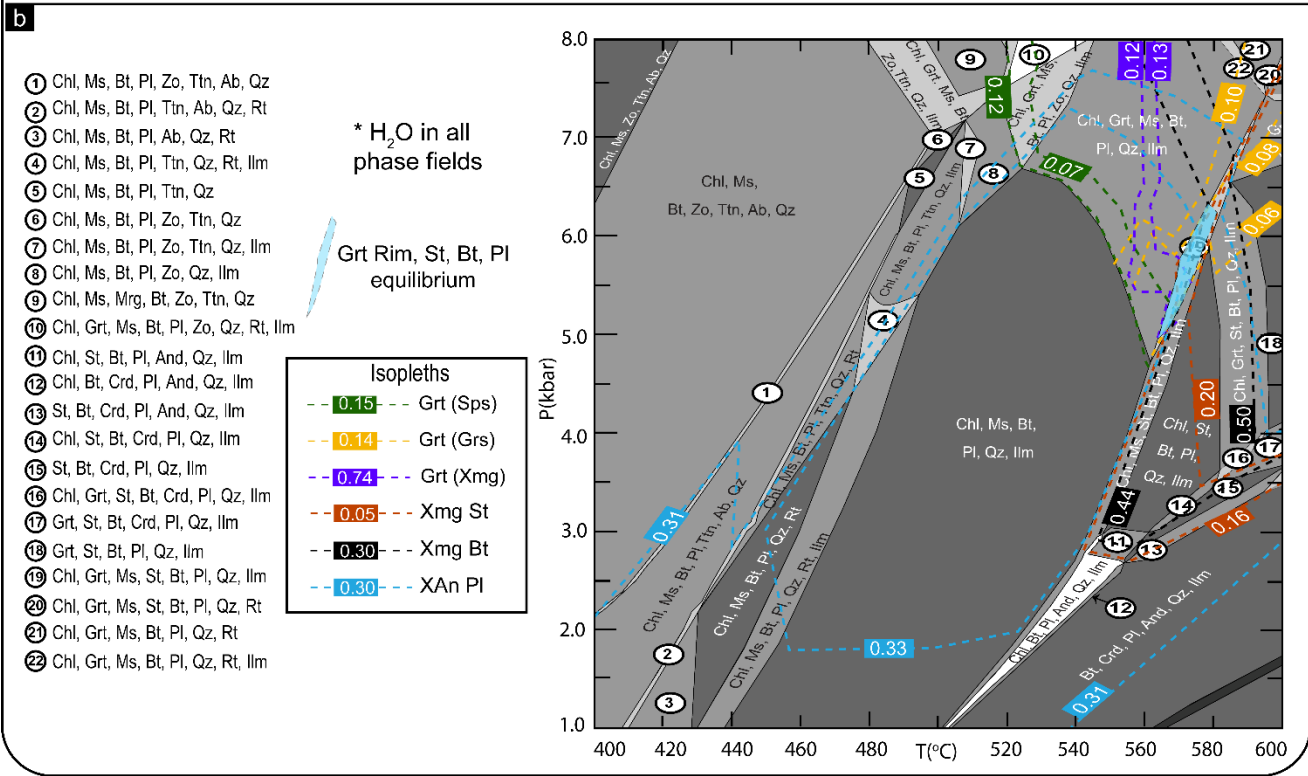
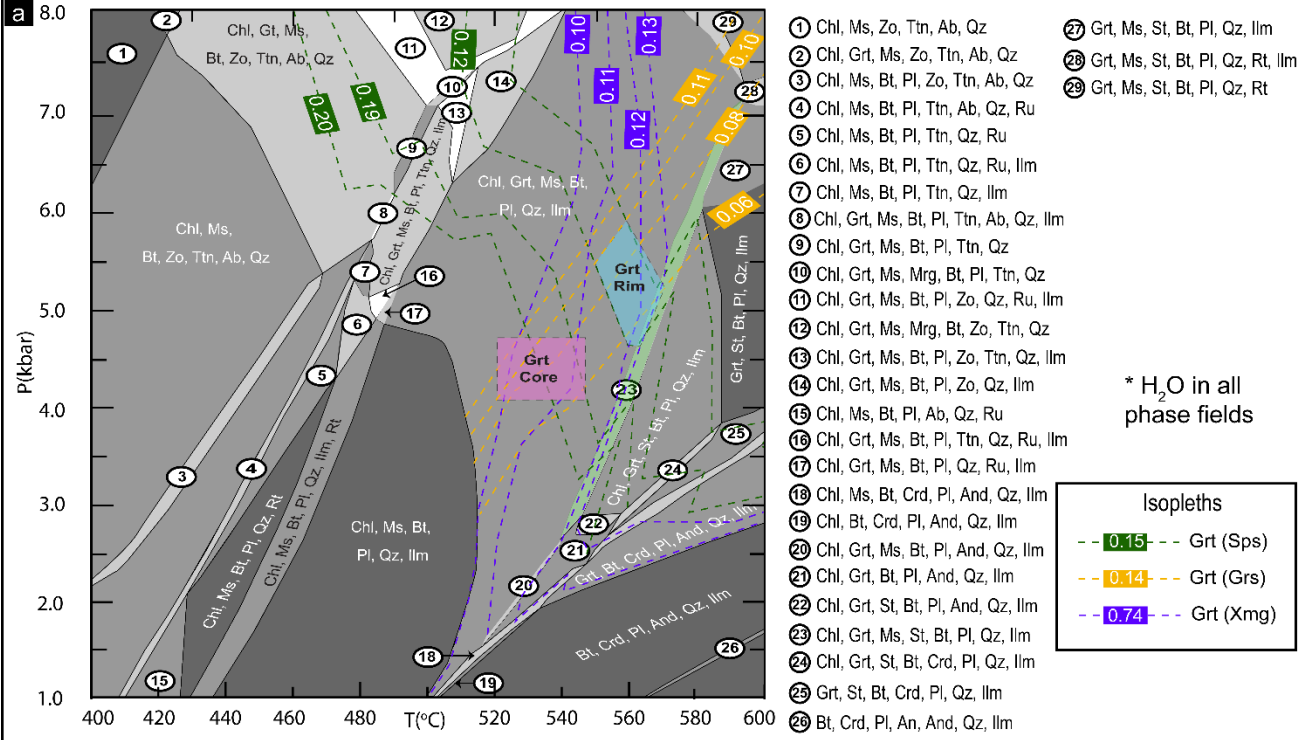
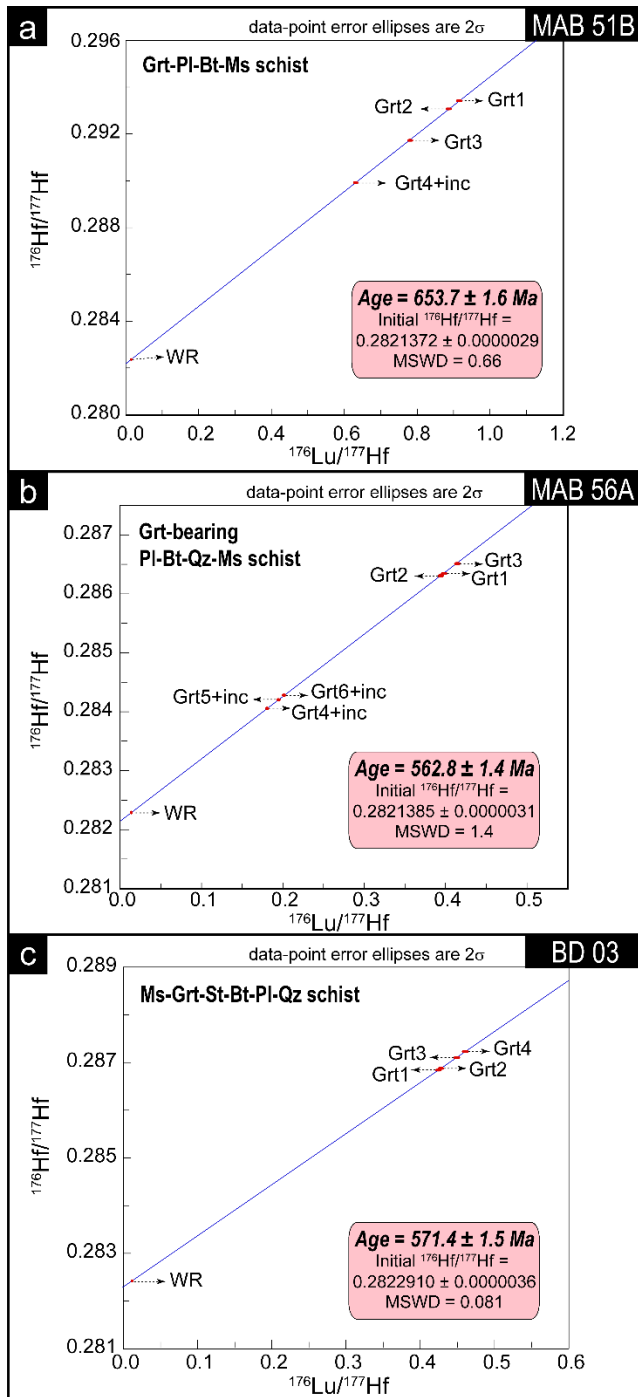
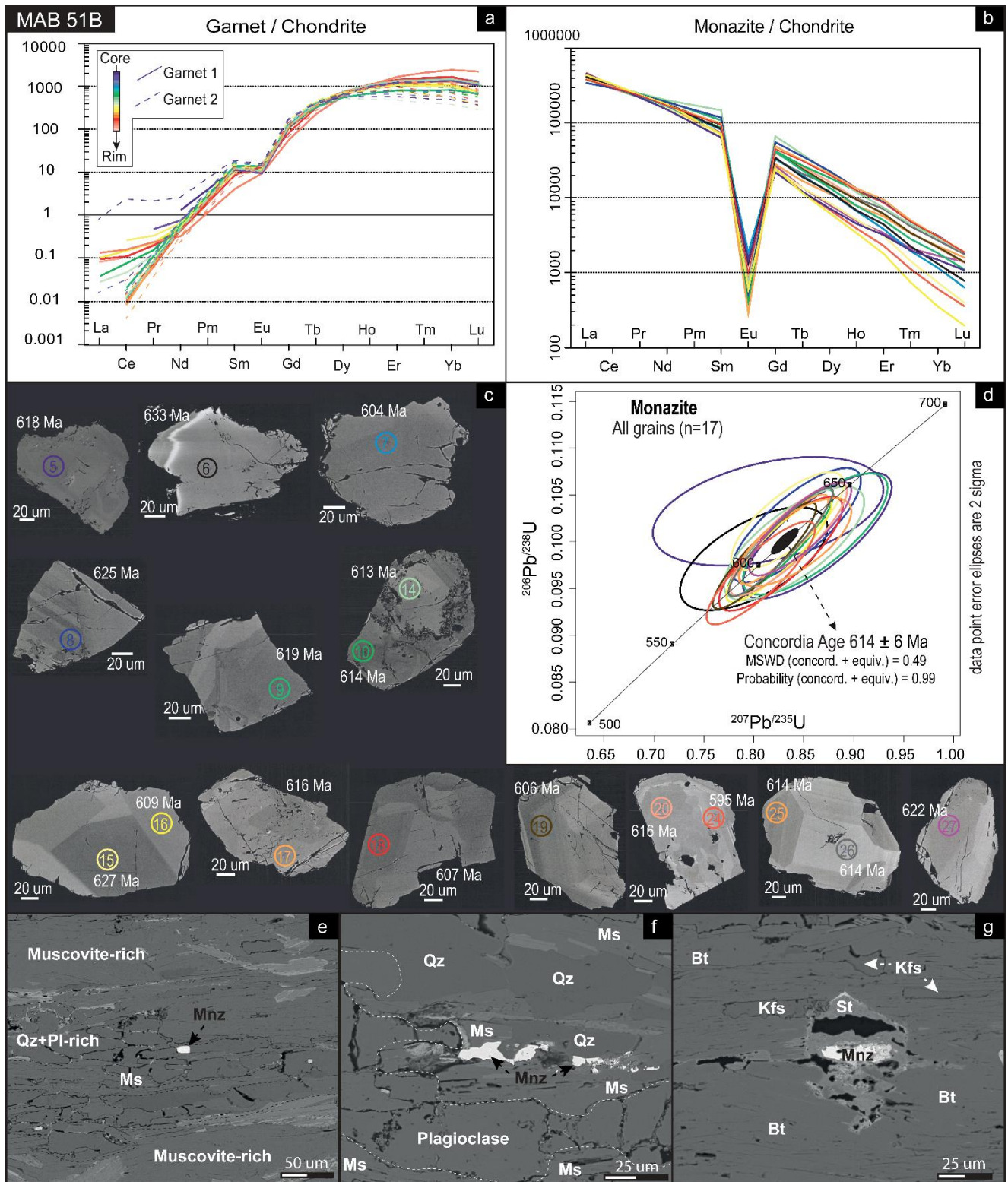


Figure 5



**Figure 6**



**Figure 7**

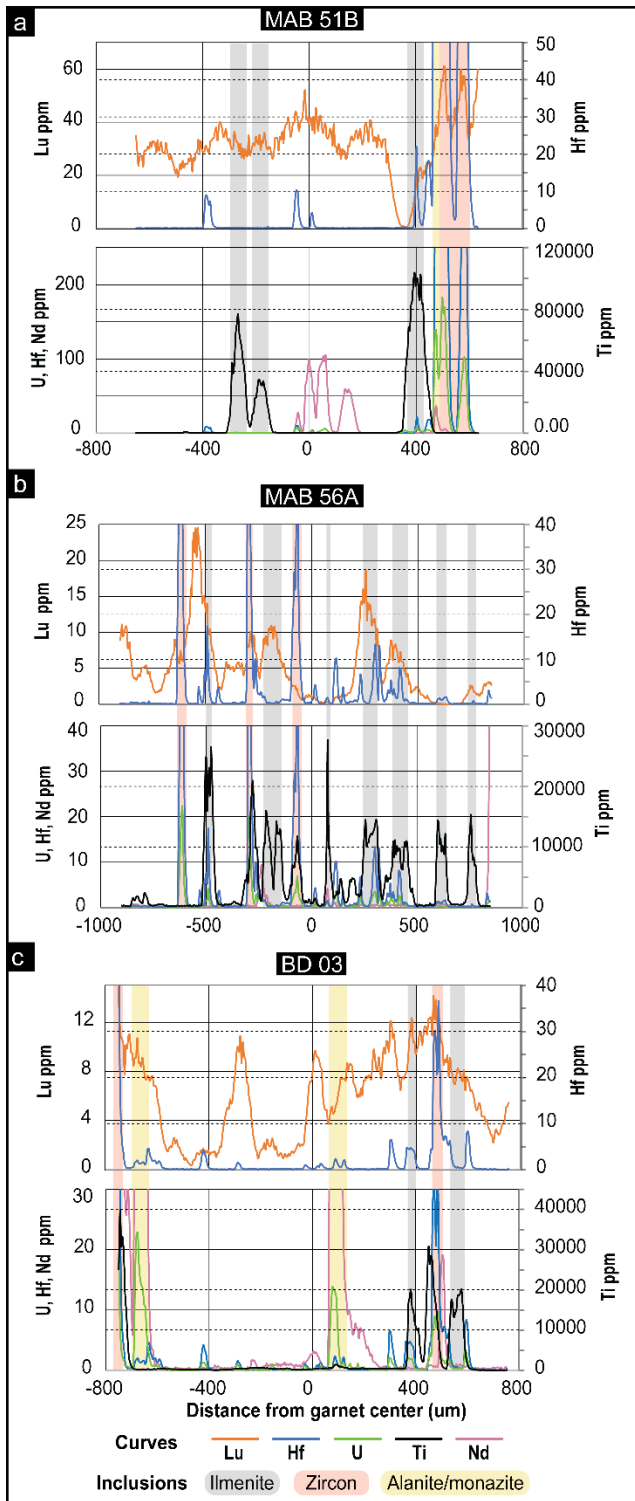


**Figure 8**



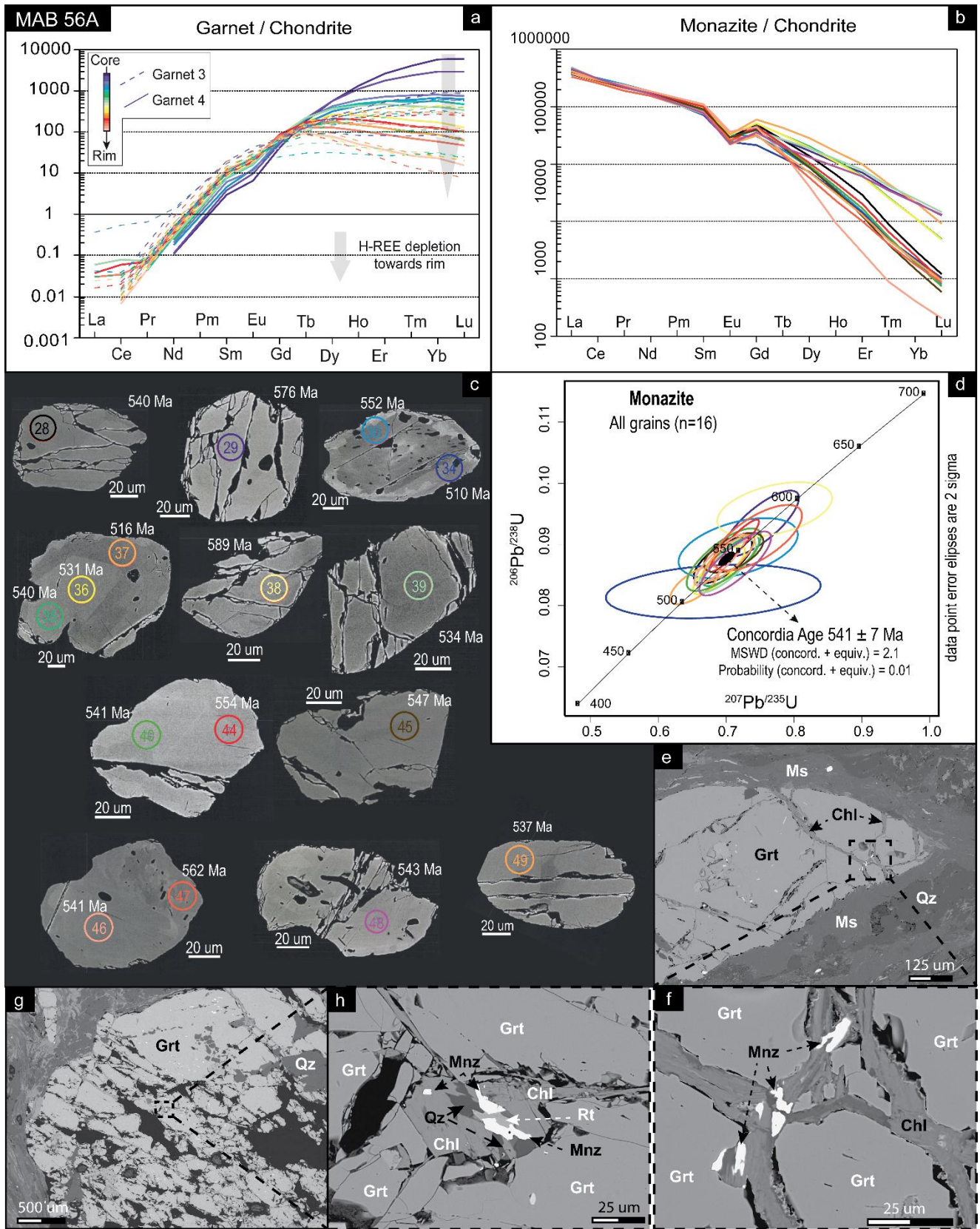
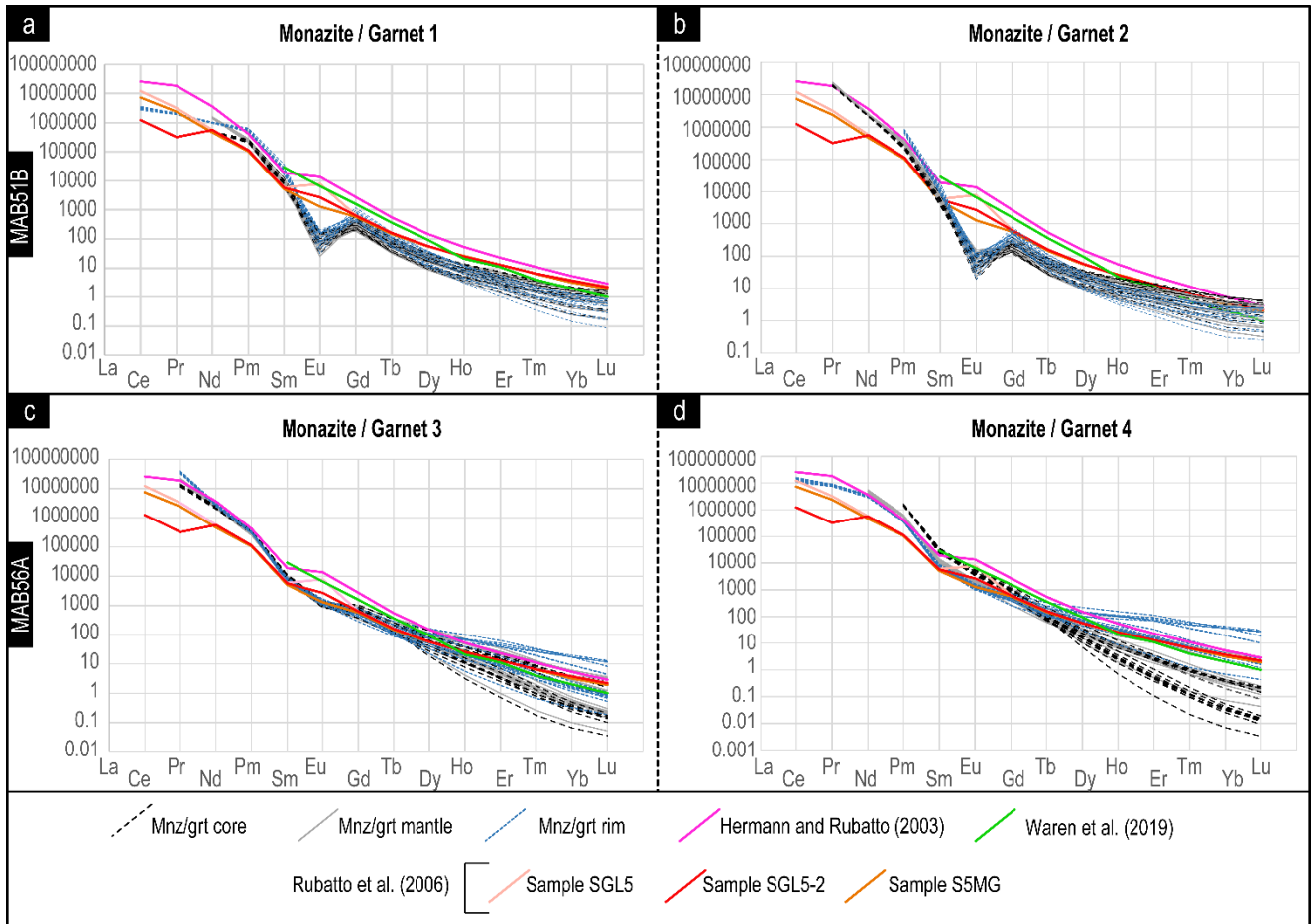


Figure 9



**Figure 10**





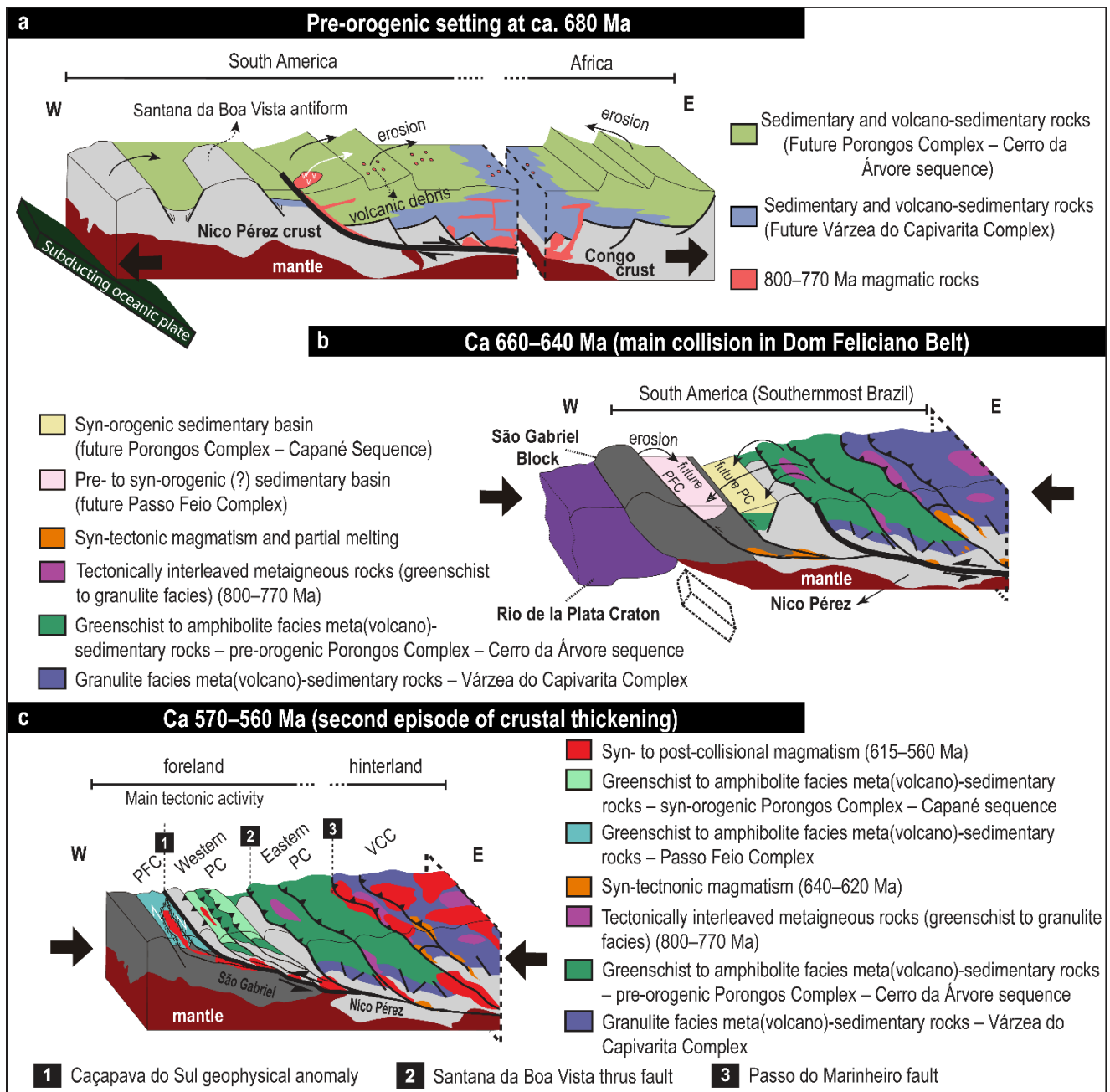


**Figure 12**

Table 1. Representative microprobe analyses of minerals (The analyses were recalculated based on the following nr. of oxygen atoms: PI = 8O; Bt, Ms = 11O; Grt = 12O; Chl = 14O; St=24O). All analyses are available as supplementary data.

Sample	MAB56A						BD03						
	Wt%	Bt	Ms	Pl	Chl	Grt core	Grt rim	Bt	Ms	Chl	Pl	St	Grt core
SiO <sub>2</sub>	33.75	45.11	68.04	24.71	37.46	37.22	35.60	45.75	24.74	59.95	27.65	36.75	37.46
TiO <sub>2</sub>	1.90	0.30	0.05	0.07	0.08	0.05	1.19	0.45	0.13	0.03	0.67	0.05	0.07
Al <sub>2</sub> O <sub>3</sub>	20.49	36.90	20.32	21.66	21.03	20.79	19.91	37.13	23.29	24.63	53.66	20.68	21.20
FeO	22.90	1.03	0.19	31.60	31.09	36.50	18.03	0.73	23.48	0.08	13.37	28.97	33.86
MnO	0.07	0.02	-	0.20	5.60	1.20	0.10	0.04	0.17	0.00	0.19	8.45	3.14
MgO	6.82	0.35	0	10.10	1.38	2.12	10.01	0.56	15.02	0.00	1.73	1.78	2.91
CaO	0	0	0.10	0.03	3.86	2.54	0.00	0.01	0.02	6.95	0.04	2.98	2.39
Na <sub>2</sub> O	0.16	1.24	11.97	0.02	-	-	0.16	1.23	0.00	7.95	0.03	0.00	-
K <sub>2</sub> O	8.41	9.21	0.01	-	-	-	9.06	9.41	0.03	0.10	0.00	0.00	-
Cr <sub>2</sub> O <sub>3</sub>	0.10	0.07	-	0.08	0.13	0.02	0.09	0.18	0.03	0.00	0.06	0.00	0.00
ZnO	-	-	-	-	-	-	0.00	0.00	0.00	0.00	0.15	0.00	-
<b>Total</b>	<b>94.58</b>	<b>94.26</b>	<b>100.68</b>	<b>88.55</b>	<b>100.63</b>	<b>100.43</b>	<b>94.12</b>	<b>94.84</b>	<b>86.92</b>	<b>99.68</b>	<b>97.55</b>	<b>99.65</b>	<b>101.04</b>
Si	2.62	3.02	2.96	2.67	3.01	3.00	2.71	3.02	2.62	2.67	3.93	2.99	2.99
Al <sup>IV</sup>	1.38	0.98	1.04	1.33			1.29	0.98	1.38	1.32	0.07	0.01	0.01
Al <sup>VI</sup>	0.50	1.92	0	1.50	1.99	1.98	0.50	1.91	1.51	0	8.92	1.98	1.99
Cr	0.01	0	-	0.01	0.01	0.00	0.01	0.01	0	0	0.01	0.00	0.00
Fe <sup>3+</sup>	0	0	-	-	-		0	0	-	0	0	0.02	-
Ti	0.11	0.02	0.001	0.01	0.00	0.00	0.07	0.02	0.01	0	0.07	0.00	0.00
Fe <sup>2+</sup>	1.49	0.06	0.01	2.85	2.09	2.46	1.15	0.04	2.08	0	1.59	1.95	2.26
Mn	0.01	0	-	0.02	0.38	0.08	0.01	0.00	0.02	0	0.02	0.58	0.21
Mg	0.79	0.04	0	1.63	0.17	0.25	1.14	0.05	2.37	0	0.37	0.22	0.35
Ca	0	0	0.01	0.003	0.33	0.22	0	0.00	0	0.33	0.01	0.26	0.20
Na	0.02	0.16	0.99	0.01	-	-	0.02	0.16	0	0.69	0.01	0.00	-
K	0.83	0.79	0.001	-	-	-	0.88	0.79	0	0.01	0.00	0.00	-
Zn	-	-	-	-	-	-	0	0	0	0	0.02	0.00	-
X <sub>Mg</sub>	<b>0.35</b>	<b>0.39</b>	-	<b>0.36</b>	<b>0.07</b>	<b>0.09</b>	<b>0.50</b>	<b>0.58</b>	<b>0.53</b>	-	<b>0.19</b>	<b>0.10</b>	<b>0.13</b>
X <sub>An</sub>	-	-	<b>0.99</b>	-	-	-	-	-	-	<b>0.32</b>	-	-	-
X <sub>Grs</sub>	-	-	-	-	<b>0.11</b>	<b>0.07</b>	-	-	-	-	-	<b>0.09</b>	<b>0.07</b>
X <sub>Alm</sub>	-	-	-	-	<b>0.70</b>	<b>0.82</b>	-	-	-	-	-	<b>0.65</b>	<b>0.75</b>
X <sub>Py</sub>	-	-	-	-	<b>0.06</b>	<b>0.08</b>	-	-	-	-	-	<b>0.07</b>	<b>0.11</b>
X <sub>Sps</sub>	-	-	-	-	<b>0.13</b>	<b>0.03</b>	-	-	-	-	-	<b>0.19</b>	<b>0.07</b>

Table 2. Summary of estimated PT conditions and comparison of observed vs. modelled mineral compositional parameters.

Sample	PT estimates					Mineral Compositions								
	T (°C)		P (kbar)			X <sub>Alm</sub>	X <sub>Spss</sub>	X <sub>Prp</sub>	X <sub>GrS</sub>	Grt X <sub>Mg</sub>	Bt X <sub>Mg</sub>	Chl X <sub>Mg</sub>	X <sub>An</sub>	St X <sub>Mg</sub>
	min max	mean	min max	mean										
MAB56A core	520	<b>530</b>	3.9	<b>4.6</b>	Obs.*	0.74	0.09	0.06	0.11	0.08	-	-	-	-
	540		5.3		Mod.♣	0.72	0.10	0.05	0.12	0.07	-	-	-	-
					% diff.	-2	+1	-1	+1	-1	-	-	-	-
MAB56A rim	545	<b>555</b>	4.3	<b>4.8</b>	Obs.*	0.79	0.04	0.08	0.09	0.09	0.34	0.37	1.00	-
	565		5.3		Mod.	0.81	0.02	0.08	0.09	0.09	0.32	0.39	0.89	-
					% diff.	+2	-2	0	0	0	-2	+2	-11	-
BD03 core	525	<b>535</b>	4.1	<b>4.3</b>	Obs.*	0.65	0.20	0.07	0.08	0.10	-	-	-	-
	545		4.5		Mod.♣	0.65	0.20	0.08	0.07	0.11	-	-	-	-
					% diff.	0	0	+1	-1	+1	-	-	-	-
BD03 rim	560	<b>570</b>	4.7	<b>5.6</b>	Obs.*	0.73	0.10	0.10	0.07	0.12	0.49	0.52	0.32	0.18
	580		6.5		Mod.♣	0.77	0.05	0.10	0.08	0.12	0.41	0.50	0.50	0.18
					% diff.	+4	-5	0	+1	0	-8	-2	+18	0

\* Median values shown for observed mineral compositions ♣ Modelled mineral compositions calculated using mean PT estimates

Table 3. Summary of the Lu–Hf dating results.

Sample	Fraction	Weight (mg)	Lu (ppm)	Hf (ppm)	<sup>176</sup> Lu/ <sup>177</sup> Hf	Error	<sup>176</sup> Hf/ <sup>177</sup> Hf	Error	Age (Ma)
MAB51B	Grt1	60.80	24.11	3.65	0.9167	0.0458387	0.2934	0.0000031	654±2
	Grt2	59.77	24.42	3.81	0.8879	0.0443961	0.2930	0.0000024	
	Grt3	60.23	23.61	4.19	0.7820	0.0391048	0.2917	0.0000039	
	Grt4+inc.	190.89	25.91	5.68	0.6323	0.0316155	0.2899	0.0000025	
	WR	31.75	0.73	6.77	0.0148	0.0007436	0.2823	0.0000027	
MAB56A	Grt1	61.05	7.88	2.74	0.3981	0.0199052	0.2863	0.0000031	563±1
	Grt2	60.18	7.60	2.68	0.3938	0.0196920	0.2863	0.0000048	
	Grt3	91.16	8.06	2.70	0.4144	0.0207188	0.2865	0.0000049	
	Grt4+inc.	64.30	6.45	4.96	0.1805	0.0090225	0.2840	0.0000036	
	Grt5+inc.	208.00	7.13	5.08	0.1946	0.0097286	0.2842	0.0000025	
	Grt6+inc.	192.72	7.26	5.00	0.2015	0.0100729	0.2842	0.0000043	
	WR	29.92	0.54	5.42	0.0137	0.0006862	0.2823	0.0000059	
	WR	31.47	0.53	5.37	0.0137	0.0006851	0.2823	0.0000035	
BD03	Grt1	100.80	12.15	3.97	0.4246	0.0212277	0.2868	0.0000017	571±2
	Grt2	100.56	11.63	3.77	0.4280	0.0213986	0.2869	0.0000031	
	Grt3	123.17	12.54	3.87	0.4495	0.0224754	0.2871	0.0000035	
	Grt4	121.95	12.15	3.66	0.4606	0.0230301	0.2872	0.0000029	
	WR	30.13	0.42	4.31	0.0135	0.0006776	0.2824	0.0000028	

All errors are 2 SE (standard errors) and relate to the last significant digits. Constants used for data reduction: <sup>179</sup>Hf/<sup>177</sup>Hf=0.7325 (Patchett and Tatsumoto, 1980) and the exponential law were used for mass bias correction of interfering Yb and Lu isotopes and isotopes of Hf; <sup>176</sup>Lu decay constant = 1.867x10<sup>-11</sup> (Söderlund, 2004). Grt = garnet; WR = Whole-rock; Grt+inc = garnet with inclusions.



Table 4. Comparison of the P–T estimates from the Porongos and Passo Feio complexes presented in this paper with the data available in the literature.

Complex	Sample	Early garnet growth	Metamorphic peak	Garnet + whole rock age (Ma)	Monazite age (Ma)	Reference	
Porongos	Eastern region	<b>MAB 51B</b>		<b>654±2</b>	<b>614±6</b>	<i>This paper</i>	
		MAB 52A	555–565 °C at 5.4–5.7 kbar	560–580 °C at 5.8–6.3 kbar	-	-	De Toni et al. (2021)
		CMP13 CMP54		584 ± 50 °C at 5–6 kbar	658±26 (Rb–Sr, Ms–WR)	-	Lenz (2006)
	Northwestern region	<b>MAB 56A</b>	520–540 °C at 3.9–5.3 kbar	Ca. 545–565 °C at 4.3–5.3 kbar	<b>563±1</b>	-	<i>This paper</i>
			<b>Greenschist facies (retrogression)</b>		-	<b>541±7</b>	
	Passo Feio	<b>BD 03</b>	525–545 °C at 4.1–4.5 kbar	560–580 °C at 4.7–6.4 kbar	<b>571±2</b>	-	<i>This paper</i>
BD 16C		490–500 °C at 2.5–3.3 kbar	500–510 °C at 5–6.4 kbar	-	-	Costa et al. (2021)	
BD 15		530–550 °C at 3.0–4.3 kbar	560–570 °C at 5–5.5 kbar	-	-		